

UNIVERSITY OF CRETE
DEPARTMENT OF PHYSICS

MASTER THESIS

**Development of high temperature single
photon emitters based on InAs piezoelectric
quantum dots**

Author:
Ioannis THYRIS

Supervisors:
Prof. Z. HATZOPOULOS
Prof. N. PELEKANOS

Heraklion
October, 2017

Contents

Contents	i
Acknowledgements	
Motivation	1
1 Theoretical Background	3
1.1 Excitons and Biexcitons	3
1.2 Growth	4
1.3 Fine Structure Splitting	6
1.4 Piezoelectric Effect	7
2 Quantum dots in a Short Period Super-Lattice	9
2.1 Simulation	10
2.2 Experimental	12
2.2.1 Sample 1503	14
2.2.2 Sample 1552	15
2.2.3 Sample 1553	15
2.2.4 Sample 1554	17
2.2.5 Sample 1555	18
2.2.6 Sample Comparison	18
3 Quantum dots in a Cavity	23
3.1 Theoretical Aspects	23
3.1.1 Signal Gain	25
3.2 Experimental	29
3.2.1 Sample 1508	31
3.2.2 Surface Degradation	32
3.2.3 Sample 1509	34
3.2.4 Sample 1572	34
3.2.5 micro-PL	35
4 Quantum dot capping with Aluminum Arsenide	42
4.1 Experimental	43
4.1.1 Reference Samples	44
4.1.2 1ML AlAs capping	45
4.1.3 0.5ML AlAs capping	45
4.1.4 0.6ML AlAs capping	47

4.1.5	0.3ML AlAs capping	48
4.1.6	micro-PL	49
4.1.7	AlAs-capping QD Samples on Semi-Insulating Substrates	50
	Future Work	52
	Bibliography	53

Acknowledgements

In these few lines I would like to take the opportunity to thank all the people who have contributed in the present thesis, both directly and indirectly.

First and foremost, I would like to express my gratitude to my supervisor Prof. Nikos Pelekanos for the guidance he provided and his patience with me. He was willing to assist even with the most trivial experimental tasks and answer the most trivial questions. His insight on the subject and the many fruitful discussions we had were invaluable for grasping the subject and writing this text.

Next, I would like to thank Prof. Zacharias Hatzopoulos and Prof. Georgios Kopidakis for being in the supervising committee. I would also like to thank Prof. Zacharias Hatzopoulos for the growth of all the MBE samples presented in this thesis and for giving insight on the growth procedure.

The work of this thesis would not be possible without the contribution of Maria Androulidaki, who helped me in the lab and shared her expertise on optical measurements and optical elements. Next, I would like to thank Charalambos Katsidis for the introduction to the nextnano³ software package. I would also like to thank Katerina Tsagaraki for the AFM and EDX characterization and the SEM pictures, as well as Antonis Stavrinidis and George Constantinidis for the fabrication of micropillars, the corresponding SEM pictures and for sharing the process flow of the fabrication.

A special thanks goes to Savvas Germanis. Even though not present in Heraklion, the knowledge he acquired around the micro-PL setup was ever-present. I also thank him for the crucial hands-on help he provided during his one week vacations in Crete. Additionally, I would like to thank all the Microelectronics Research Group members and all the students with whom we shared the lab or the office, for giving useful advice and for the everyday cooperation.

Words cannot describe my gratitude towards my family for always believing in me and for always supporting me during my studies. I would also like to thank my friends who were always there to laugh and have a good time. Next, I would like to thank my partner Fotini for giving me courage and for being my “stress-repellent”.

Last but not least, I owe a “thank you” to the tango community of Heraklion for embracing me and for providing an environment to relieve stress and express myself.

Motivation

Up until a few decades ago, information had been viewed only in classical terms, in which quantum theory remained on the sidelines and only had the role of designing the equipment to process it and set limitations on the speed of transmission. However, quantum mechanics have now come into play and the quantum nature of information offers considerable benefits over classical information, such as in quantum computing, making the tackling of certain mathematical problems way faster, and quantum cryptography, the security of which lies on fundamental physics. The corresponding bit in quantum information is called qubit (quantum-bit) and is, in general, a microscopic system with two distinguishable states. Such candidate systems are atoms or nuclei with the qubit being the spin-1/2 states and photons with the qubit represented by the two photon polarization states. The latter case is particularly promising because photons can propagate quickly in optical fibers over long distances without losses.

The realization of qubits based on the two orthogonal photon polarization states requires reliable single-photon sources [1]. Such sources have been demonstrated with atoms [2], molecules [3], nitrogen vacancy centers in diamond [4] and from quantum dots (QDs) [5]. Quantum dots, nanostructures of a semiconductor material, which have already been used as an active region for lasers [6], offer advantages as candidate single-photon sources.

However, any practical use of a single-photon emitter would require performance at elevated temperatures, making most of the systems above unsuitable. Quantum dot systems that operate at high temperature are II-VI systems, up to 220K for (Cd,Zn)Se QDs [7] and GaN/AlN QDs up to room temperature [8]. It is important, however, in order to have a single-photon device, to be able to electrically pump the QDs, in which GaAs-based QDs are the best candidates, due to the already available technological know-how. Using optical pumping, single-photon emission of up to 120K has been reported [9], while using electrical pumping single-photon emission up to 77K has been achieved [10]. The next temperature milestone is that of thermoelectric coolers operating at around 220K, which are commercially available, compact and low-cost compared to the liquid helium and liquid nitrogen conditions required for the single-photon emission presently. In this direction, the piezoelectric QDs examined in the present thesis, can potentially achieve single-photon emission at that much elevated temperatures due to particular properties, which will be briefly mentioned in the Theoretical Background chapter.

Additionally, an important role in quantum information schemes play the so-called, entangled states, with which we can, for example, connect distant points in space-time by distributing keys over long distances. These states are two-qubit states, which cannot be factorized into a product state of the two qubits and are in the core of quantum communica-

tion and quantum computing developments. Again, QDs are good candidates as a source of entangled photon pairs, with piezoelectric quantum dots bearing a striking advantage over their non-piezoelectric counterparts. This advantage is that piezoelectric QDs is that they can have very small fine structure splittings (FSS), a quantity that will be explained briefly in the Theory chapter. In (100), people have manipulated FSS by annealing [11], by applying magnetic fields [12], electric fields [13], strain [14] etc. Such schemes are cumbersome, making piezoelectric QDs are more appealing candidate for entanglement, shown from (111) Qds in inverted pyramids [15].

Chapter 1

Theoretical Background

A semiconductor quantum dot, or QD for short, is a nano sized structure of a semiconductor material which is embedded in the matrix of another semiconductor material, the band gap of which is larger than the QD semiconductor. More generally, a quantum dot can be considered as a reduced dimensionality system. By the term reduced dimensionality we mean that, in contrast to the bulk material, the carriers are spatially confined in a number of dimensions. Such structures are Quantum Wells (QWs), where the carrier confinement occurs in one dimension, Quantum Wires, where electrons and holes are confined in two dimensions and Quantum Dots, where the carriers are confined in all three dimensions. The number of dimensions in which the mobility of the carriers is constrained defines the dimension of the structure. As a result, QWs are two-dimensional, Quantum Wires are one-dimensional and QDs are zero-dimensional structures. The 3D confinement of electrons and holes inside a quantum dot gives rise to a discrete energy spectrum, as depicted in the delta function-like density of states (DOS) in Fig. 1.1. Due to both the localization of the carriers and the discrete transition energies, a quantum dot is often called as an “artificial” atom, even though each QD is made from a large number of atoms, in the order of tens of thousands.

1.1 Excitons and Biexcitons

An electron and a hole can form an unstable bound quasi-particle called exciton (X) [16], due to their Coulomb interaction. The excitons formed in the bulk material are called free excitons. However, excitons do not only form in the bulk material. When an electron and a hole are inside the quantum dot, thanks to their Coulomb interaction, they form excitons which are spatially confined in the QD. In general, excitons are divided in Frenkel and Wannier excitons, depending on their coupling strength. In the case of InAs QDs, we are interested in Wannier excitons, whose coupling strength is relatively weak and the excitons span over many unit cells. Being unstable, after a short period of time of the order of nanoseconds, the exciton decays. Free excitons can decay both radiatively and non-radiatively. However, in good quality crystals, QD excitons formed from an electron and a hole in the ground state of the conduction and valence band of direct band gap semiconductors respectively, mostly decay radiatively, emitting a photon of energy $\hbar\omega_X$. As

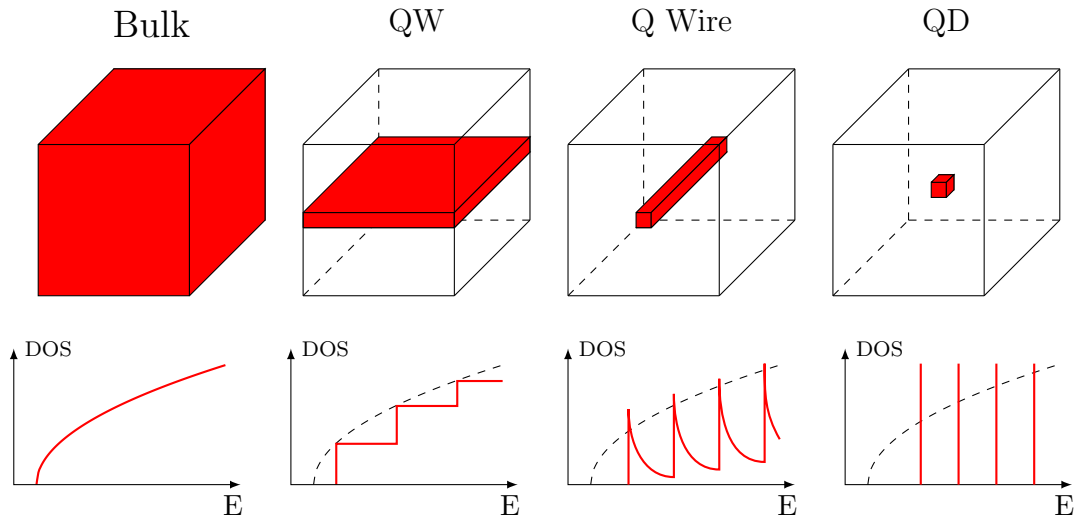


Figure 1.1: Structures of reduced dimensionality and their corresponding density of states, compared to the bulk material. The QD density of states is discrete, in contrast to the others, the DOS of which is continuous.

in atoms, following Pauli's exclusion principle, two electrons at maximum, with opposite spins, can occupy the QD conduction band ground state. The same applies for holes in the valence band. As a result, the QD ground state has a maximum of two electrons and two holes. The quasi-particle formed due to the Coulomb interaction between two electrons and two holes in the QD is called biexciton (XX). The biexciton decays to the exciton state through the recombination of an electron-hole pair, emitting a photon of energy $\hbar\omega_{XX}$. The difference between $\hbar\omega_X$ and $\hbar\omega_{XX}$ is called the biexciton binding energy. The biexciton binding energy is nonzero because the electron-hole recombination in the biexciton takes place under the influence of the other two charges, in contrast to the single exciton recombination. The other occupation combinations in the QD ground state involve an odd number of electrons and holes, and the corresponding quasi-particles are called trions. The case where there are two electrons and one hole, or more conveniently, one exciton and one electron is called a negatively charged exciton or negative trion (X^-). When the opposite occurs, one exciton and one hole occupy the ground state, the quasi-particle is called positively charged exciton or positive trion (X^+). Trions decay through electron-hole recombination and emit photons of energies $\hbar\omega_{X^-}$ and $\hbar\omega_{X^+}$ respectively, both of which differ from their corresponding neutral exciton (X). The corresponding energy transitions of the exciton, biexciton and trions can be seen in single QD spectroscopy and the identification of each one is often a non-trivial task.

1.2 Growth

This thesis is focused on (211)B InAs self-assembled quantum dots, which are grown using molecular beam epitaxy, on a GaAs substrate. The letter B indicates that the crystal is terminated with the As face. The lattice constant of InAs is 7% larger than the lattice

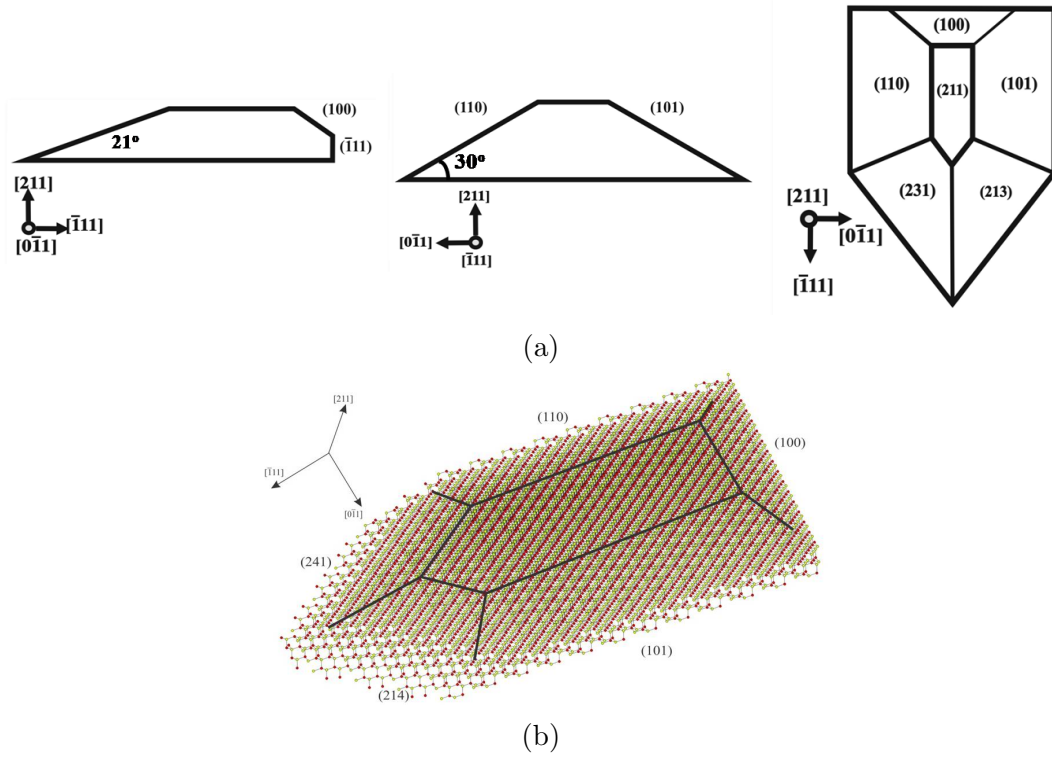


Figure 1.2: (a) Cross sectional illustrations of (211)B InAs quantum dots along $[0\bar{1}1]$, $[\bar{1}11]$ and $[211]$ respectively. (b) Atomistic model of the InAs QD, showing a faceted pyramidal shape.

constant of GaAs. The QDs are formed using the Stranski-Krastanov (S-K) growth mode [17]. Atoms impinge on the GaAs substrate and a two-dimensional InAs thin film is initially formed. As the 2D thickness increases, the strain on the layer increases as well, due to the lattice mismatch. Above a critical thickness, the strain is relaxed through the formation of three dimensional islands, i.e the dots. This is a phase transition from layer by layer growth to cluster formation. In other words, above the critical thickness, the system is in a lower energy state when QDs are formed, in contrast to accumulating strain when growing layer by layer. Of course, this process depends highly on the growth conditions, such as the growth temperature and growth rate. The 2D layer which is left after the formation of QDs, is called the wetting layer (WL). For the QD formation in the (211)B direction, temperatures of $\sim 450 - 530^\circ C$ are required for the S-K transition. At lower temperatures, the indium adatoms are not mobile enough to form the 3D island and the strain is relaxed through the introduction of misfit dislocations. At higher temperatures, on the other hand, the impinging indium atoms cannot be adsorbed by the surface as easily. In contrast to (100) InAs QDs, their (211)B counterparts exhibit a narrower range of conditions capable of QD formation. The shape of the dots, depending on the growth conditions, may take the form of truncated pyramids or “quantum dashes” [18]. For the growth conditions used in this thesis, the dots take the form of truncated pyramids [19], as shown in Fig. 1.2. The typical dot height is $\sim 2 - 3 \text{ nm}$, while the typical dot diameter is $\sim 30 - 40 \text{ nm}$. All of the samples mentioned in this work were grown with the S-K growth mode, but the growth conditions

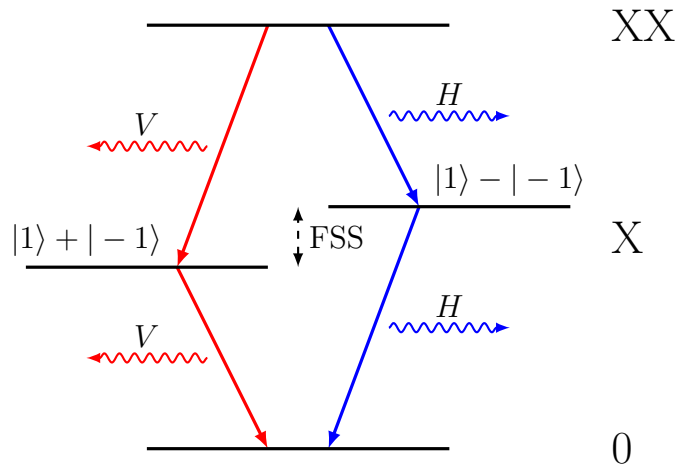


Figure 1.3: The biexciton cascade of a QD with low confinement potential symmetry. The biexciton decay has two distinguishable paths, each producing photons with perpendicular polarization to the other. In dots where the confinement potential is highly symmetric, the FSS is close to zero and the two paths become indistinguishable.

were varied depending on the wanted QD size and QD density and as a result the growth conditions of each sample will be mentioned when the sample is presented, throughout this text.

1.3 Fine Structure Spitting

Electrons and holes trapped inside QDs interact electrostatically and form excitons which are unstable bound quasi-particles. The exciton energy levels are determined by the spin configurations of the electron and the hole that form it. The excitonic state with the lowest energy is realized as a superposition between an electron and a heavy hole, having an angular momentum of $s = \pm 1/2$ and $j = \pm 3/2$, respectively. Thus, the total angular momentum of the exciton produced can be either $M_{dark} = \pm 2$ or $M_{bright} = \pm 1$ [20]. An exciton in the bright state ($M = \pm 1$) decays radiatively and a photon of spin ± 1 is emitted. On the other hand, this is not possible for the dark state ($M = \pm 2$), which cannot couple with the light field. Normally, these four states would be degenerate, but the presence of electron-hole exchange interaction splits the dark states from the bright states and mixes the two dark states, forming a dark doublet ($|2\rangle \pm |-2\rangle$), as well as the two bright states forming the bright doublets ($|1\rangle \pm |-1\rangle$). The two bright doublets' degeneracy is lifted by the anisotropy of the confinement potential in combination with the exchange interaction. The ground state is the symmetric linear combination, while the asymmetric linear combination has higher energy.

The energy difference corresponding to the two bright states ($|1\rangle \pm |-1\rangle$), is called the exciton fine structure splitting (FSS). This is a measure of the confinement symmetry. As the confinement potential becomes more and more asymmetric, the value of FSS increases. The biexciton states do not have a fine structure splitting, due to the fact that the total spin of the carriers involved is zero. The FFS of a positively charged exciton state is zero as

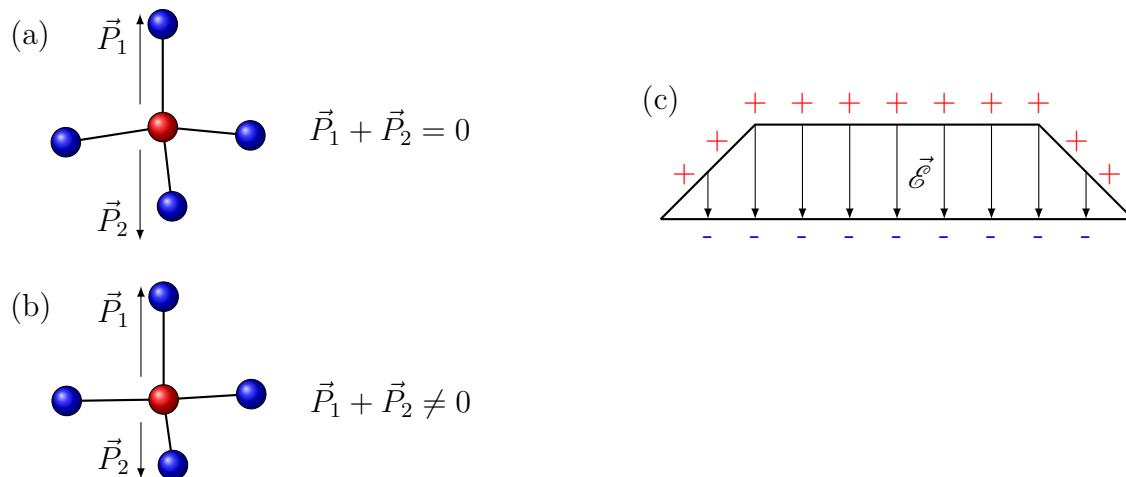


Figure 1.4: (a) When no strain is present, the atoms in the zinc-blende lattice form a tetrahedron and the total polarization is zero. (b) When strain is applied, the bond geometry is perturbed, resulting in non-zero polarization. (c) The positive and negative dipole moments cancel out in the bulk of the QD, leaving only bound charges on the surface of the QD, which produces the piezoelectric field.

well, due to the fact the the charged state can be viewed as an electron interacting with a spin-singlet electron-hole pair [12]. By the same logic, the negatively charged exciton state has no FSS too. The fine structure splitting affects the biexciton cascade, as shown in Fig. 1.3. The biexciton decay has now two well-defined paths, due to non-zero FSS. Each path produces photons, the linear polarization of which is perpendicular to the polarization of the photons produced from the other path. For a highly symmetric confinement potential, the FSS vanishes. This makes the two decay routes indistinguishable and thus, systems that have low FSS values, are good candidates for the generation of polarization entangled photon pairs, which are of crucial importance in quantum optics and quantum communication experiments. It has been shown that in systems that exhibit high piezoelectric fields along the growth direction, such as QDs on high index substrates (eg. (111) or (211)), the confinement potential symmetry is preserved and as a result, the FSS values can be close to zero [21, 22]. The piezoelectric effect, an important feature of our QDs, will be presented in more detail in the next section.

1.4 Piezoelectric Effect

As already indicated in the title of this thesis, the quantum dots that we examine are piezoelectric QDs, in the sense that they exhibit an intrinsic piezoelectric field along the growth direction. Before we go into further detail how this field affects the QD characteristics, we give a brief explanation of the piezoelectric effect in the Zinc Blende lattice.

In general, when lattice mismatched heterostructures are grown on substrates with polar crystallographic orientation (N11), a piezoelectric field is produced. This strain induced polarization of the material is called the piezoelectric effect. For the sake of clarity, we demonstrate the situation along the (111) direction. When the lattice is strain-free, the

chemical bonds between the III-V ions form a tetrahedron. Because of the geometry of the bonds, the contribution on the polarization from the top bond cancels out the contribution from the three bottom, resulting in a zero net polarization (Fig. 1.4a). However, when the system is perturbed under strain, the bonds are deformed, resulting in an induced dipole moment, as shown in Fig. 1.4b.

For the (211)B case, which is misaligned to (111) by $\sim 19.5^\circ$, the same logic applies. In the case of heterostructures, there exist a large number of such dipoles. In each dipole, the negative charge is neutralized by the presence of positive charge from the adjacent dipole. As a result, in a piezoelectric QD there are only surface charges of opposite sign at the base and the apex, which give rise to the piezoelectric field, shown in Fig.1.4c. This field is predicted to get its maximum value for the (111) orientation, with the value for (211) being weaker but not too far off [23]. However, the fabrication of (111) QDs is not a trivial task and requires special methods [15, 24]. For a more complete picture of the piezoelectric effect, one must include both the ionic and the electronic response to the imposed strain [25]. However, the simplistic model used here, taking into account only ionic response, provides a basic understanding of the phenomenon.

The presence of the piezoelectric field changes the electronic and optical properties of the QD. The confinement potential is altered due to the field, and the conduction and the valence bands bend, resulting in a spatial separation of electrons and holes, reducing their respective wave-functions overlap. This phenomenon, present when electric fields are applied in nanostructures, is called the Quantum Confined Stark Effect. The electron states shift to lower energies and the hole states shift to higher energies, which in consequence red-shifts the exciton transition energy. The biexciton transition energy is shifted, as well, due to the presence of the surface charges. In other words, when the biexciton decays to the exciton state, the electron-hole recombination now does not only occur under the influence of the other electron-hole pair, but also in the presence of the piezoelectric field, and the net outcome is typically a shift of the biexciton line to higher energy with respect to the exciton.

In this chapter we gave a brief and general introduction to the quantum dot theoretical background needed to follow this thesis. Most of the work here is based on the above background and lies behind the conception of the topics in the following chapters. However, since the notions presented in this chapter are rather broad and specific theoretical considerations are needed, each subsequent chapter will also have a theory section, dedicated to the topic of the specific chapter.

Chapter 2

Quantum dots in a Short Period Super-Lattice

The development of realistic quantum cryptography and quantum computation technologies requires sources operating at high temperatures that emit single and entangled photons “on demand” [1]. Of all the candidate systems we are specifically interested in the arsenides-based quantum dots, as explained in the introduction. The record-holding single photon emitters using (100) InAs quantum dots operate at temperatures up to 120K [9]. In the (211)B direction single photon emission at up to $\sim 150K$ has been previously achieved in our lab. However, raising the operating temperature of a single photon emitter is not a trivial task to accomplish. In this chapter, we present a key feature towards high temperature single photon emission, which is called short period super-lattice, or SSL for short. A brief introduction to SSLs is given first and their use is initially justified by doing a simple 1D simulation on nextnano³ [26], a simulation software of nanostructures. Then, the experimental results of the SSL sample series will be presented and discussed.

The limiting factor of high temperature luminescence from quantum dots is the thermal activation of carriers out of the dot [27]. To be more specific, when an exciton is formed, the electron and the hole can escape to the surroundings of the dot, by acquiring enough thermal energy, where it is likely to find alternative non-radiative recombination paths, instead of relaxing back into the dot. As a result, the electron-hole pair cannot recombine to emit single photons at the selected energy. By surroundings, we mean the bulk of the semiconductor, but most importantly the wetting layer (WL) on which the dots are formed. The wetting layer is a thin InAs-based layer which is formed when the indium atoms impinge on the surface during growth, before the transition to 3D nucleation. The average energy of the carriers needed in order for them to be thermally activated is called activation energy, providing a measure on how easily the carriers escape to the WL. As a result, the main idea is to grow structures which have high activation energies, requiring higher temperatures for the thermalization of the carriers. In other words, we want to make sure that the carriers stay confined inside the dot in order to recombine and emit a photon. In fact, we want to make it as difficult as possible for them to escape. By doing so, we make our dots more robust at higher temperatures.

In previous studies [27], it was shown that the activation energy E_{act} to the wetting

layer can be related to the emission energies of the dot E_{QD} and the wetting layer E_{WL} respectively. In fact, the activation energy is found to be equal to: $E_{act} \equiv \Delta E = E_{WL} - E_{QD}$. Consequently, in order to increase the activation energy to the wetting layer, we must increase ΔE . One way to achieve this is to grow bigger dots, which would redshift their PL emission, while leaving the WL transition energy intact. However, this has the drawback of making the dots prone to having more dislocations, making our dots less optically active. In addition, our CCDs have a wavelength cut-off at about 1050 nm , so we are limited by our lab equipment as well. The other option available, which is the one we chose in this work, is to shift the WL emission to higher energies. One way to achieve this is by embedding our QDs between AlGaAs pseudo-alloys. These pseudo-alloys are made from binary GaAs/AlAs short period super-lattices (SSLs). The composition of the SSLs is: a $m\text{-\AA}$ thick layer of GaAs, followed by a $n\text{-\AA}$ thick layer of AlAs, which are repeated for κ periods. The SSL acts presumably as an $\text{Al}_{x'}\text{Ga}_{1-x'}\text{As}$ alloy with x' varying depending on the values m and n as: $x' = n/(m+n)$. Note that the x' is used for the alloy corresponding to the SSL, while x is reserved for the real alloy. The reason behind the use of the SSL instead of an $\text{Al}_x\text{Ga}_{1-x}\text{As}$ barrier is that the crystal quality of $\text{Al}_x\text{Ga}_{1-x}\text{As}$ in the (211)B direction is relatively poor due to growth-related difficulties in the (211)B direction. Previous attempts on growing (211)B InAs QDs on $\text{Al}_x\text{Ga}_{1-x}\text{As}$ in our lab were not very successful. The attempts to grow the dots directly on AlAs were not successful either, for similar reasons. It seems that the dots prefer their formation on GaAs. As a result, using GaAs/AlAs short period super-lattices with the GaAs layer adjacent to the dots does the trick of having the dot nucleation and having the necessary effective barrier to increase ΔE .

2.1 Simulation

In this section we attempt to establish the use of the SSL and demonstrate its key concepts by doing 1D simulations using nextnano³ [26]. The software nextnano³ allows us to simulate nanostructures and extract useful information, such as the eigenenergies of the system by solving a 1D Schrödinger equation in the envelope function approximation. In the simulation, we have included both strain and piezoelectric effects in the (211)B orientation. Here, we chose to use a 1D simulation and to ignore the lateral dimensions due to the large aspect ratio of the dots (diameter to height ~ 10), meaning that the quantum confinement is much stronger in the growth direction [19].

In the first simulation, we check that the SSL indeed behaves like a barrier of varying height, depending on the thicknesses of the GaAs and AlAs layers. The results are shown in Fig.2.1. For the calculation, we have used a constant AlAs thickness of $n = 16\text{\AA}$ and varied the GaAs thickness between $m = 24\text{\AA}$ and $m = 8\text{\AA}$ with a step of 4\AA . The simulation is done for 10 and 20 periods of the SSL. The band gap of the SSL is taken to be the first transition energy in the Γ point (e1-hh1) and its effective composition factor is given by $x' = n/(n+m)$. The transition remains direct in k-space in the whole range. As evident the SSL acts as a barrier, the height of which increases as the GaAs layer thickness decreases. Additionally, there seems to be no significant difference between 10 and 20 periods of the SSL in our simulation. The band gap of a real $\text{Al}_x\text{Ga}_{1-x}\text{As}$ is plotted in the same scale, for comparison. Attention has been given to include the band gap at the Γ point, because the

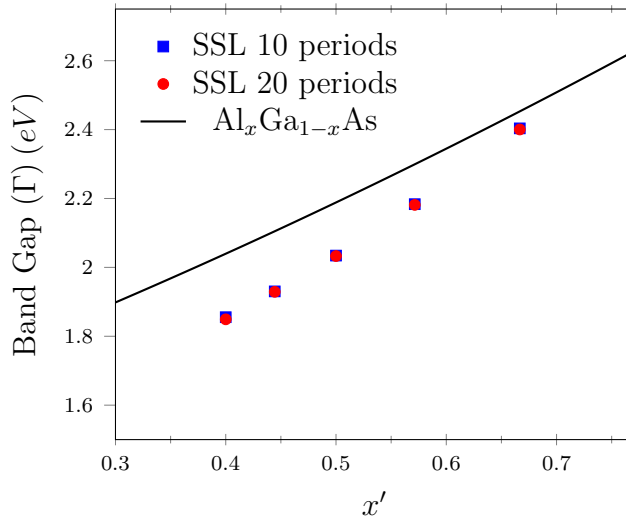


Figure 2.1: Plot of the SSL band gap for 10 and 20 periods in comparison to the $Al_xGa_{1-x}As$ band gap. The SSL band gap is given by the e1-hh1 transition energy extracted from the simulation, while the $Al_xGa_{1-x}As$ band gap is given for the Γ point. The points for 10 and 20 periods practically coincide.

$Al_xGa_{1-x}As$ band gap becomes indirect at $x > 0.44$. The SSL band gap seems to roughly follow the $Al_xGa_{1-x}As$ band gap trend. However, the SSL with effective composition x' cannot be simply considered as $Al_{x'}Ga_{1-x'}As$, as the band gap difference varies from $0.19 eV$ at $x' = 0.4$ to $0.05 eV$ at $x' = 0.67$. To compare, the SSL with $x' = 0.5$, corresponds to an $Al_xGa_{1-x}As$ barrier with $x = 0.4$.

In the next simulation, we check whether the presence of the SSL increases $\Delta E = E_{WL} - E_{QD}$, as claimed in the introduction of the chapter. The idea behind the use of the SSLs is that the presence of the SSL barriers affects the WL emission much more effectively than the dot emission. This can be seen by doing a simple 1D simulation using nextnano³. In this simulation both WL and the QD are seen as $In_xGa_{1-x}As$ wells in the growth direction. The intermixing of the dot occurs due to gallium atoms entering the dot from the layer on which they are grown. This effect, called surface segregation, will be the subject of the last chapter of this thesis. However, the width of the WL well is smaller than that of the dot, as shown in Fig.2.2b. In fact, in our case the WL thickness is taken, based on HR-TEM results [19], to be $\approx 0.8 nm$, while a typical QD height is $\approx 3 nm$. We used $Al_{0.5}Ga_{0.5}As$ as a simplification of the dot composition profile extracted in reference [19]. Both WL and QD is sandwiched between two ten period SSLs of constant AIAs thickness 16 \AA , while the GaAs thickness varies between $m = 24 \text{ \AA}$ and $m = 8 \text{ \AA}$ with a step of 4 \AA ($x' = n/(n+m)$). As seen from the previous simulation, the dependence on the periods of the SSL is small and only the ten period case has been considered. The transition energies (e1-hh1) for both cases are plotted in Fig.2.2a for the different GaAs layer thicknesses. The dashed lines represent the transition energy in the absence of the SSL. It is obvious that as the barrier increases the shift of the transition energy is greater in the WL compared to the dot. To be precise, the transition shift of the WL, in reference to the transition energy when no SSL is present, is $\sim 0.24 eV$ while the corresponding shift for the dot is only $\sim 0.05 eV$.

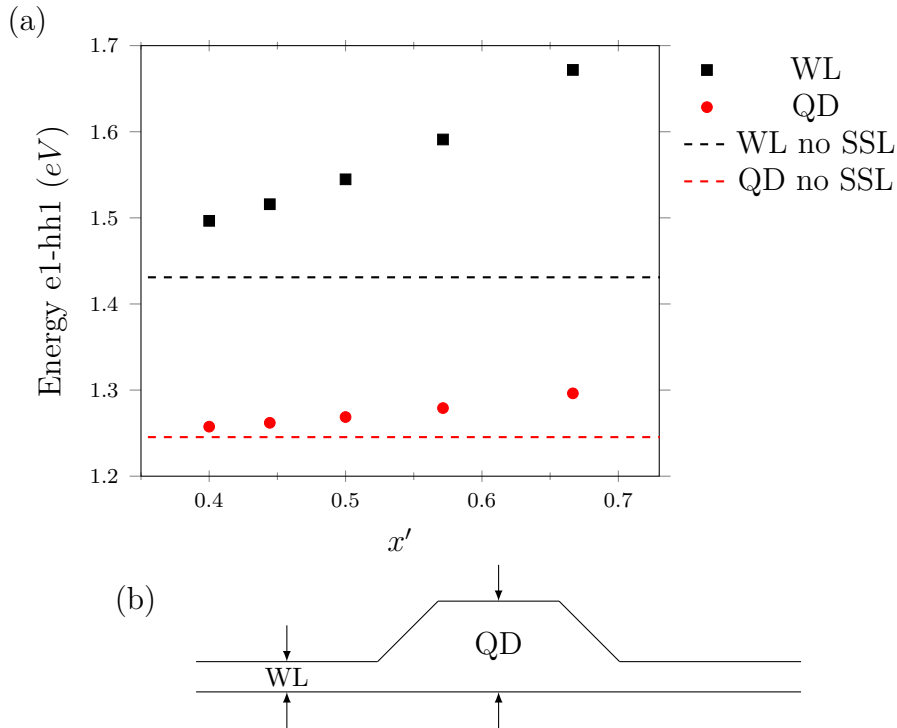


Figure 2.2: (a) Plot of the transition energies of the wetting layer and the quantum dot ground state, which are viewed as $\text{In}_{0.5}\text{Ga}_{0.5}\text{As}$ wells with width 0.8 nm and 3 nm respectively. The dashed lines represent the transition energies of the WL and the dot, assuming no barrier is present. (b) Schematic representation of the WL and QD wells along the growth axis.

The above simulations provide useful insight on the use of SSL as well as the demonstration of the reasoning of why the concept works. After making the use of SSL more concrete and vigorous, we are now ready to present the experimental work done with the short period super-lattice samples.

2.2 Experimental

We now advance to the experimental part of this chapter. Using the reasoning presented in the chapter introduction, a series of samples were grown, in which the QDs are embedded in the middle of two SSLs. A schematic representation of the samples is shown in Fig. 2.3. For all samples the same methodology has been used. After growth, the samples were characterized using photo-luminescence (PL). The PL mapping is taken, i.e. the position dependent PL, following which the temperature dependent PL is measured. Using the PL spectra obtained, the samples are evaluated and the activation energy is extracted.

The samples were grown on the MBE system of MRG at IESL-FORTH dedicated to the growth of arsenides. The substrates are epi-ready, i.e. no chemical treatment is required. The growth chamber has a vacuum of up to 10^{-11} mbar before growth starts. The growth is done under arsenic rich conditions. The As flux remains constant throughout the growth, while the growth rates are determined by the beam equivalent pressure. After the substrate

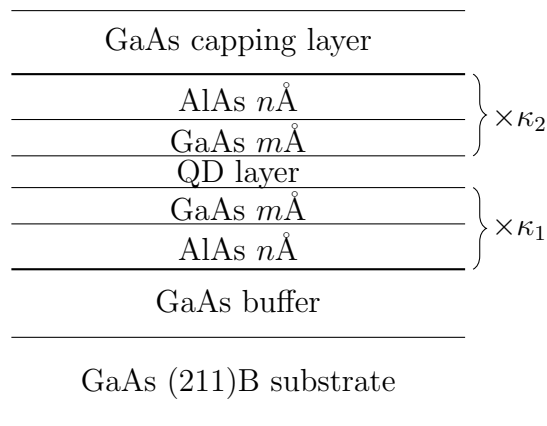


Figure 2.3: Schematic representation of our sample structures. The quantum dots are grown between two GaAs/AlAs short period super-lattices. The first SSL is repeated for κ_1 periods and the second for κ_2 . The GaAs and AlAs layer thicknesses are m and n respectively. The thicknesses of the various layers are not in scale.

is heated to 600°C and the native oxide is desorbed, the GaAs buffer layer is grown. The SSLs are grown at the same temperature. The growth rate of the GaAs layers is $0.3\text{ML}/\text{sec}$, while the AlAs layers is grown at a rate of $0.23\text{ML}/\text{sec}$. The quantum dot growth conditions will be given for each sample separately, as well as the SSL periods and layer thicknesses to highlight the differences between them. The top SSL is grown at the same temperature as the dots.

The PL characterization was performed using a continuous wave (CW) He:Cd laser, which has a wavelength of 325 nm and is focused onto the sample using a quartz lens with focal length of 10 cm . The samples were held on the cold finger of a closed-circuit helium-cooled cryostat capable of temperatures down to 12 K in vacuum conditions down to 10^{-4} mbar . The light emitted from the sample is focused using a lens with focal length of 20 cm to a spectrograph and analyzed typically with a $150\text{ g}/\text{mm}$ grating. The analyzed signal is detected using a nitrogen-cooled charge-coupled device camera (CCD). The cold finger of the cryostat can be moved using a 2D translation stage relative to the laser beam in order to obtain the PL mapping. Fluctuations of the PL signal depending on the position on the sample are due to fluctuations during growth. The temperature dependent PL is obtained by increasing the temperature in the cryostat. The temperature is raised until the dot emission is completely quenched.

Using the PL spectrum measured at each temperature, the Arrhenius plot for every sample is obtained. Each point in the Arrhenius plots is calculated as follows: A central wavelength, $\lambda_{cen}(T)$, is selected at a temperature of reference T . The reference temperature here is chosen to be 200 K , while $\lambda_{cen}(200\text{ K}) = 950\text{ nm}$, for reasons explained in the cavity chapter. Then the integrated PL intensity (I) is calculated using a spectral window of $\Delta\lambda = 4\text{ nm}$ around λ_{cen} . The integrated PL intensity is calculated at each temperature using the same $\Delta\lambda$, taking into account the dependence of $\lambda_{cen}(T)$ on temperature, which follows Varshni's law [28]. Lastly, the ratio of the integrated intensity to the maximum integrated intensity I_o is plotted in a logarithmic scale versus $1/k_B T$ and the activation

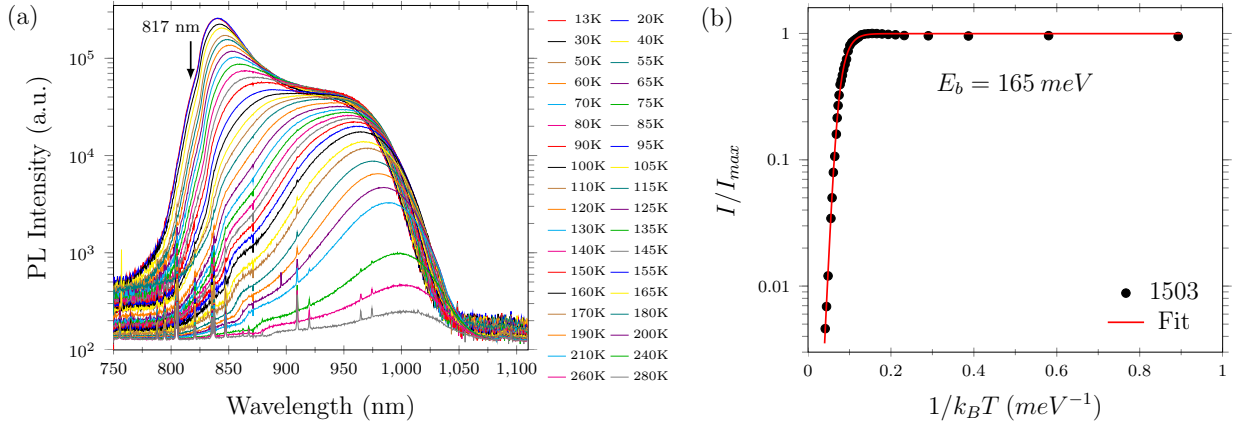


Figure 2.4: (a) The PL characterization of sample 1503. (b) The Arrhenius plot extracted from the PL of 1503 using the procedure described in the text. The activation energy to the wetting layer is found to be $E_b = 165 meV$.

energy is extracted by fitting the data with the following equation [27]:

$$I = I_o \frac{1}{1 + a \cdot e^{-E_a/k_B T} + b \cdot e^{-E_b/k_B T}}. \quad (2.1)$$

One exponential gives the activation energy due to thermalization to the WL, while the other gives the activation energy which is attributed to exciton thermalization to the p-shell of the dots. In other words, we take a family of dots that emit at $\lambda_{cen} \pm \Delta\lambda$ and we see how much their emission is sustained as the temperature increases.

2.2.1 Sample 1503

The first sample studied is labeled as 1503. The sample is grown on a semi-insulating GaAs (211)*B* substrate. After a GaAs buffer layer, which serves as a clean surface for the epitaxial growth, the first SSL is grown. The SSL consists of 16\AA AlAs and 12\AA GaAs, repeated for 50 periods. The QDs are grown directly after the SSL. The growth conditions play a critical role on the formation of the dots. The growth temperature used in this sample was $T_g = 450^\circ C$, the growth duration of the QDs was $t_g = 18 sec$ and the growth rate was $0.1 ML/sec$. After the QD layer, the second SSL is grown, which consists of 12\AA GaAs and 16\AA AlAs, repeated for 15 periods. Finally, the sample is capped with 50\AA of GaAs. The PL spectra of 1503 is shown in Fig. 2.4a. We can see some general PL characteristics, present in the QD samples. The peak centered at $\sim 840 nm$, which reduces fast with temperature, corresponds to the WL emission, while the broad emission around $950 nm$, which reduces less rapidly, corresponds to emission from the QD ensemble. Observing the PL of 1503, we can see that it has QD emission at room temperature, which is astonishing at first sight. Although this is important, what is most important is how the luminescence holds with temperature. The sample can emit at room temperature but the emission can be still quenched significantly compared to the low temperature emission. This may mean that the dots have considerable non-radiative recombination processes, according to which the excitons recombine without

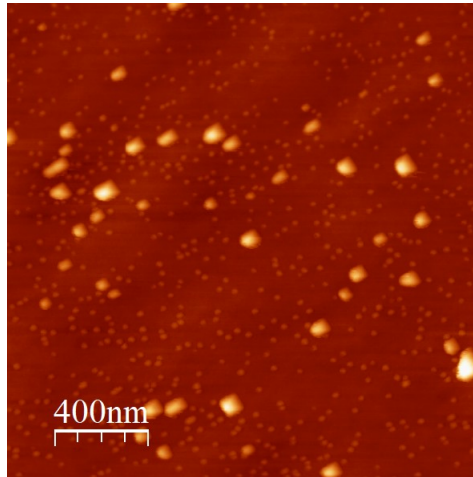


Figure 2.5: The AFM results of the sample 1552, which show successful dot growth on a SSL using the new growth conditions $t_g = 20 \text{ sec}$ and $T_g = 480^\circ\text{C}$.

emitting photons. The Arrhenius plot is shown in Fig. 2.4b. From fitting the data with Eq. 2.1, we obtain an activation energy to the WL of $E_b = 165 \text{ meV}$. This value is about 77 meV greater than the activation energies of samples without SSL. By taking into account the temperature dependence, this activation energy corresponds to a WL transition at $\sim 817 \text{ nm}$ at 13K (see arrow in Fig.2.4a), which is off by 23 nm or 52 meV compared to the WL emission from the PL obtained.

2.2.2 Sample 1552

Later, while studying AFM results from uncapped reference samples that had no SSL, it came to our attention that the samples with a growth duration of 18 seconds and $T_g = 450^\circ\text{C}$ showed relatively weaker PL and a low QD density. As a result, we increased the dot growth duration to $t_g = 20 \text{ sec}$ and the growth temperature to 480°C . By increasing the temperature to 480°C , we make the indium adatoms at the surface more energetic to find the nucleation centers, during the QD formation. The successful QD growth with these conditions is illustrated in the sample 1552, where the dots are grown on a 50 period 16\AA AlAs and 12\AA GaAs SSL. The sample is then left uncapped, i.e no other layer is grown after the dots, in order to be characterized by AFM. The AFM results are shown in Fig. 2.5. By analyzing these images we get useful information about the dot characteristics. The mean dot height is $\sim 2.5 \text{ nm}$ and the dot diameter varies between $\sim 30 - 40 \text{ nm}$. The dot density in the sample is $\sim 2 \cdot 10^{10} \text{ cm}^{-2}$. Following 1552, a capped version was grown on the same day on a second holder.

2.2.3 Sample 1553

The capped sibling of 1552 is labeled 1553 and the changes in the dot growth conditions were deployed as well. Except for the dot growth conditions which are the same as 1552, the sample is grown identical to sample 1503. The SSLs consists again of 16\AA AlAs and

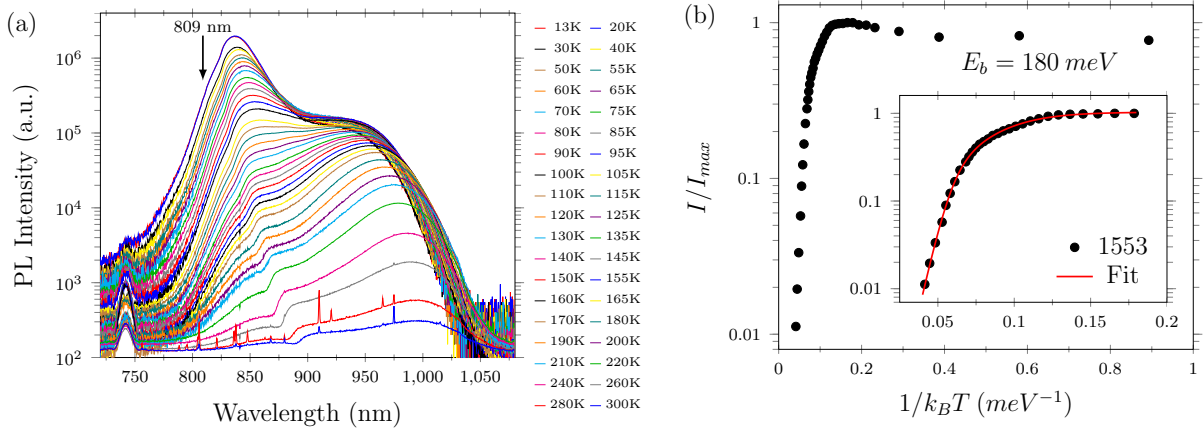


Figure 2.6: (a) The PL characterization of sample 1553, the dots of which are grown using the new conditions. (b) The Arrhenius plot extracted from the PL data of 1553. As the temperature rises from 13K to 55K, the dot emission increases as explained in the text. Inset: The activation energy extracted for sample 1554 to the wetting layer is found to be $E_b = 211$ meV.

12Å GaAs, repeated for 50 periods for the first SSL and 15 for the second one. The growth temperature of the QD layer is now $T_g = 480^\circ C$, the growth duration of the dots is $t_g = 20$ sec and the growth rate is 0.1 ML/sec. The favorable conditions for the dot formation are affirmed in the PL spectrum obtained Fig. 2.6a. From the PL of sample 1553 we can deduce a few noteworthy observations. The first one is that the PL of 1553 is much stronger compared to the PL of 1503 (assuming relatively the same focusing conditions), while the wavelength emission range is untouched, as expected from the use of the same SSL as previously. The second observation is the “inverse” peak located at ~ 823 nm at low temperatures, which red-shifts as the temperature rises. This appears in all samples of this series and could be substrate related. Another phenomenon that occurs repeatedly in QD sample emission, but is quite bizarre at first sight, is that the dot PL intensity increases as a function of the temperature up until it reaches a maximum intensity at around 70K, as shown in the Arrhenius plot of Fig. 2.6b. This can be explained by carrier localization in the WL at low temperatures which become delocalized as temperature rises, allowing additional carriers to end up inside the QDs. Both of the above characteristics appear on 1503 as well, but we chose to point them out here, where they are more prominent. In order to extract the activation energy only temperatures after the delocalization process are taken in consideration, as shown in the inset of Fig. 2.6b. The activation energy is found to be $E_b = 180$ meV. This activation energy is about 15 meV greater than the activation energy of 1503, even though the SSL used is the same. This fact could be attributed to the slightly higher WL energy in 1553, most likely due to the different growth conditions. To be more specific, in 1553 the raised growth temperature and growth duration allow the indium adatoms to find the nucleation centers much easier, leading to a slightly smaller WL thickness. Moreover, the optimized growth conditions lead to a sample with fewer defects which serve as non-radiative recombination centers and the luminescence holds better than 1503. The activation energy extracted corresponds to a WL low temperature emission at 809 nm (see arrow in Fig.2.6a), which is off by 27 nm or 49 meV from the WL peak of the

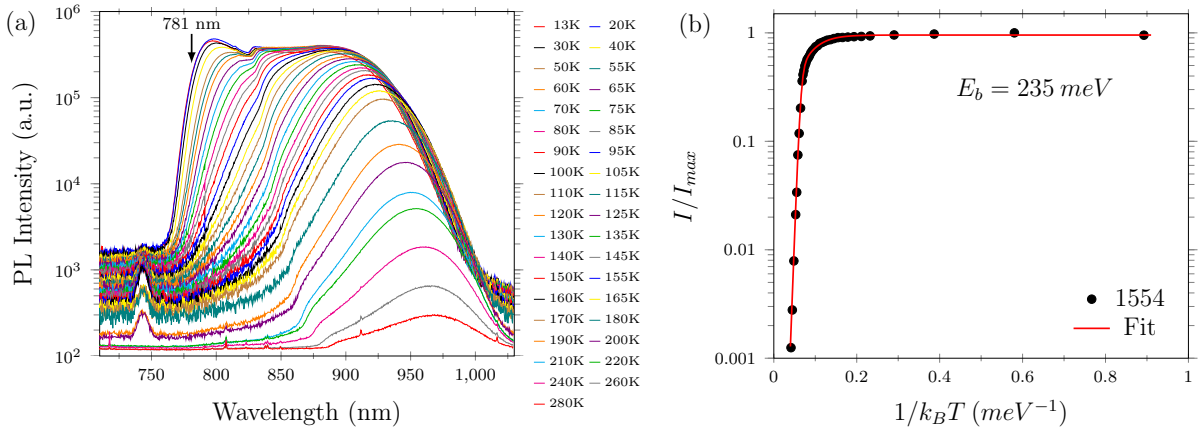


Figure 2.7: (a) The PL characterization of sample 1554, which features a high SSL barrier. (b) The Arrhenius plot extracted from the PL data of 1554. The activation energy to the wetting layer is found to be $E_b = 235$ meV.

PL spectra.

2.2.4 Sample 1554

In the next sample, labeled as 1554, the same dot growth conditions have been used, but the SSL was modified. To be more precise, the growth duration of the GaAs layer in the SSL was lowered by 14%, while that of the AlAs layer remained unchanged. The SSL now nominally consists of 16\AA AlAs and 10.3\AA GaAs, repeated for 50 periods for the first and 15 for the second SSL. Using this SSL, where the barrier is higher, we expect the emission to be shifted towards higher energies, as shown in the simulation paragraph. The growth temperature and the growth duration of the dots remain at $T_g = 480^\circ\text{C}$ and $t_g = 20$ sec respectively, while the growth rate was 0.1 ML/sec. The PL data obtained are shown in Fig. 2.7a. It is evident that the WL emission is shifted in comparison to the two previous samples by about 40 nm. The PL intensity in the dot emission range is greater than the previous samples as well, while the ratio of WL to dot emission is now ~ 1.4 , while it was ~ 7.2 and ~ 14.2 for the samples 1503 and 1553 respectively. This could be attributed to a larger QD density relatively to the other samples, but it could also mean more defects in the vicinity of the WL, which would affect its emission intensity. In Fig. 2.7b the Arrhenius plot is shown. The activation energy extracted is $E_b = 235$ meV. This translates to low temperature emission from the wetting layer at around 781 nm (see arrow in Fig.2.7a), resulting in a 16 nm or 31 meV difference between the 797 nm detected in the PL signal. It is worth mentioning that the activation energy extracted for 1554 is about 24 meV greater than the activation energy of 1553. This result is consistent with the changes made to the SSL. As we would expect, by increasing the SSL barrier we increased the activation energy.

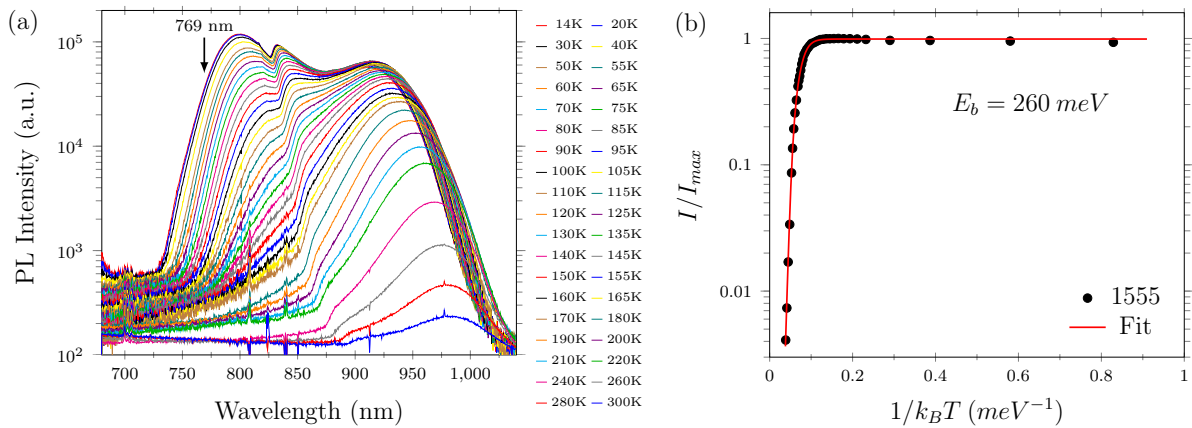


Figure 2.8: (a) The PL characterization of sample 1555, the dots of which are grown using the new conditions. (b) The Arrhenius plot extracted from the PL data of 1553. The activation energy to the wetting layer is found to be $E_b = 260\text{meV}$.

2.2.5 Sample 1555

In the quest of achieving even higher activation energies, in the next sample we lowered the GaAs layer thickness in the SSL even further. The sample called 1555 has again the same dot growth conditions: $T_g = 480^\circ\text{C}$, $t_g = 20\text{sec}$ and the growth rate being $0.1\text{ML}/\text{sec}$. However, the SSL in which the dots are embedded is slightly changed. The first SSL is repeated for 50 periods and the second for 15, but the GaAs layer thickness is reduced by 20% compared to 1553, dropping to 8.6\AA , while the AlAs layer thickness remains the same at 16\AA . The increase in the SSL barrier height, is expected to cause the emission to shift even further, compared to 1554. The PL measured is shown in Fig. 2.8a. We see that the QD emission is not shifted much, as we expected. Instead, the WL emission spectrum seems broader in the high energy side of the WL peak. The overall intensity is reduced about five-fold, which suggests an overall degradation of the sample optical quality as we reduce the SSL thickness. Nevertheless, the Arrhenius plot is shown in Fig.2.8b, with the activation energy reaching $E_b = 260\text{meV}$. This corresponds to low temperature WL emission at $\sim 769\text{nm}$ (see arrow in Fig.2.8a), marking a $\sim 29\text{nm}$ or 43meV difference between the WL emission from the PL.

2.2.6 Sample Comparison

Finally, we present a comparison between the four samples. The PL comparison is shown in Fig. 2.9. The reader should be careful when comparing the PL of the samples and not take the intensity differences as 100% exact. This is because in order to do that, we would have to measure the samples at exactly the same focusing conditions. However, this is not possible, since the samples cannot all fit in the cryostat together. As a result, we can expect that the relative signal differences from sample to sample extracted from Fig. 2.9 are different by $\sim 20\%$ from the real ones. The Arrhenius plots comparison shown in Fig. 2.10, on the other hand, is more accurate. The reason behind this is that the Arrhenius plots use relative intensities, i.e the intensities normalized by the max intensity for each sample. As a result,

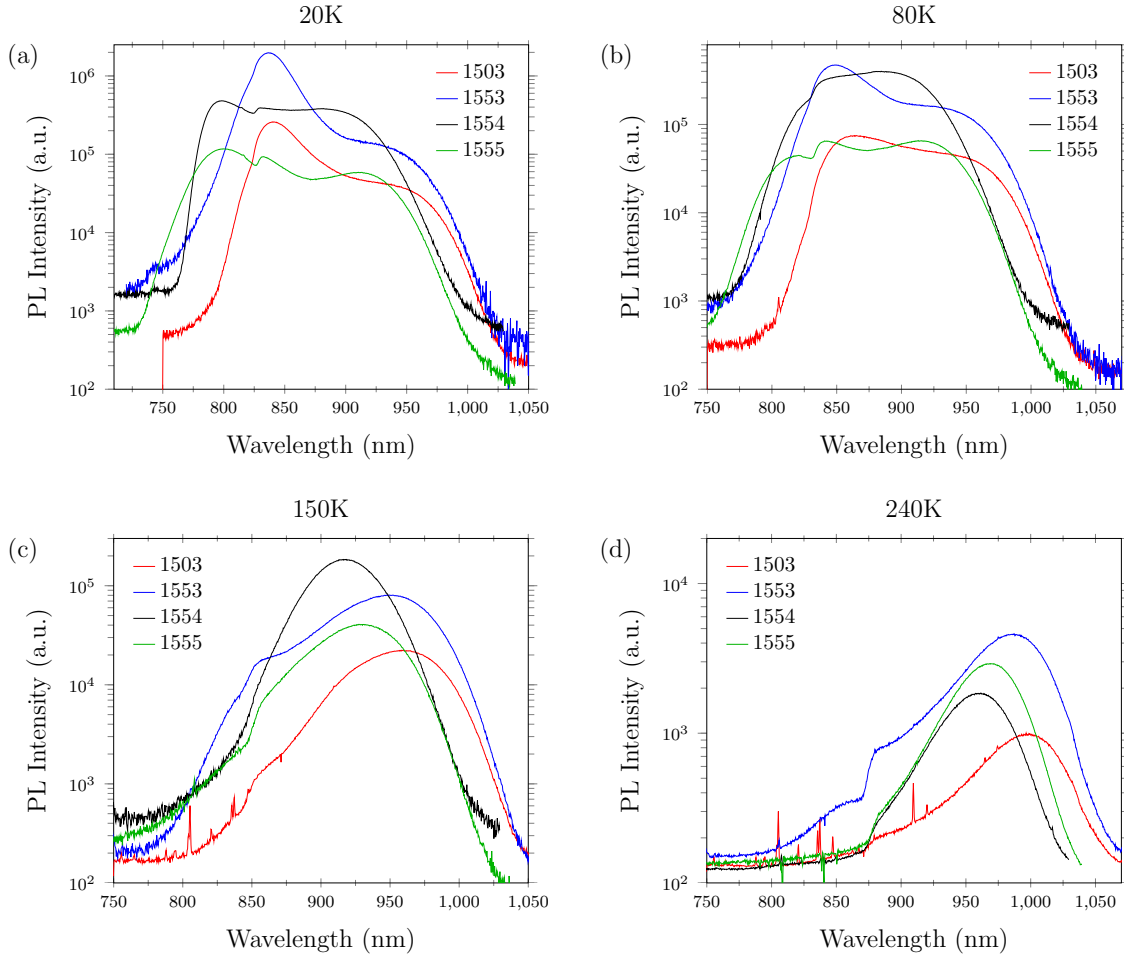


Figure 2.9: The PL comparison of our samples for different temperatures. For reasons explained in the text, we can only get a qualitative comparison on the intensity of the samples.

we can compare how the ratio quenches as the temperatures rises, regardless of whether they were measured by exactly the same focusing conditions or not.

As seen in Fig.2.9a, at 20K, samples 1553 and 1554 are the most intense, with 1553 having more intense WL emission, while 1554 has more intense QD emission. The picture remains roughly the same at 80K and at 150K, where the WL emission is completely quenched, sample 1554 has more intensity than the rest. However, the picture is drastically changed at 240K, where sample 1553 is now the most intense, with 1554 having less intensity than 1555. Something noteworthy is that 1553 is more intense at 240K, even though it has a lower activation energy than 1544 and 1555. This at first seems odd, but it becomes more clear in the Arrhenius plot comparison in Fig. 2.10. At around 150K ($1/k_B T \simeq 0.08$), we can see that the relative intensity is progressively higher as we go from 1503 to 1555. Moreover, we notice that the samples drop to half of their maximum intensities at higher and higher temperatures. To be specific, the relative intensity is quenched to half the maximum at $\sim 135K$ for 1503, at $\sim 140K$ for 1553, at $\sim 155K$ for 1554 and at $\sim 160K$ for 1555. However, as the temperature rises even further, the relative intensity is reduced at

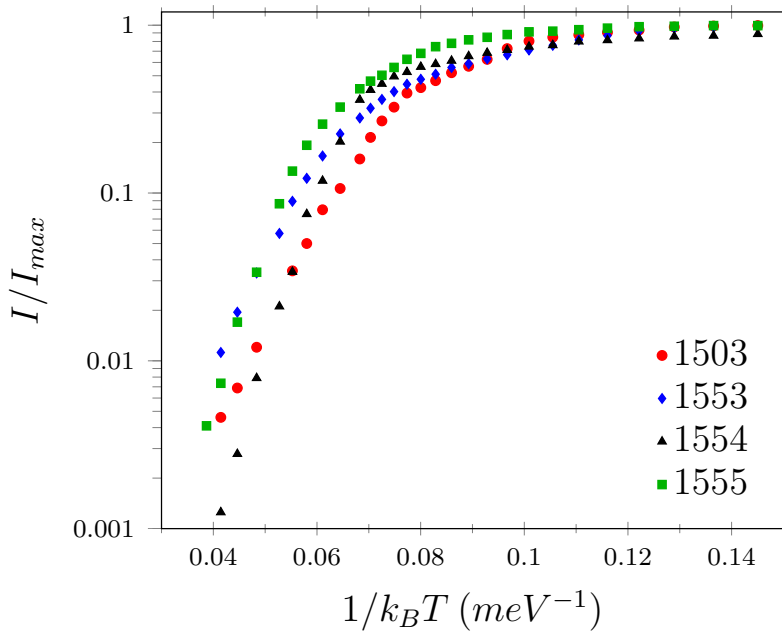
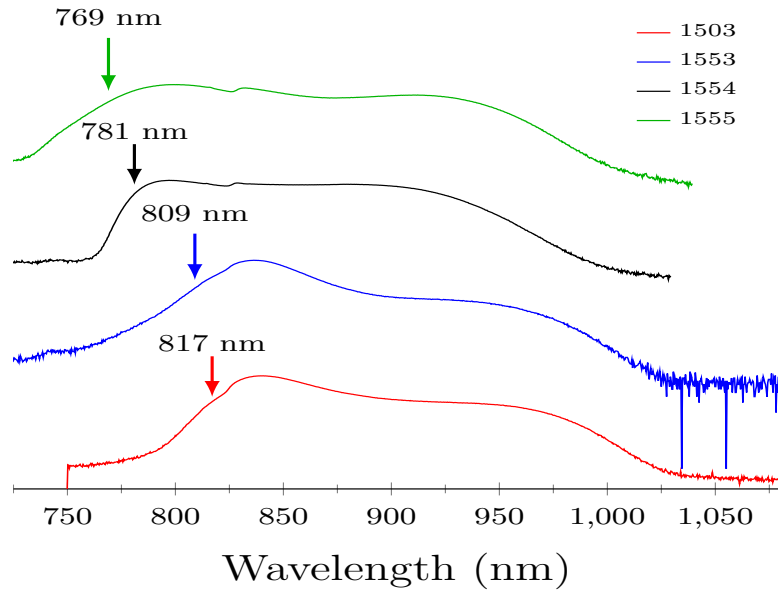


Figure 2.10: The comparison between the Arrhenius plots of our samples.

different paces for each sample. For samples 1554 and 1555 specifically, the relative intensity decreases more strongly than the two other samples. As a result, even though the relative intensities of 1554 and 1555 drops to half at higher temperature than samples 1503 and 1553, their intensities become lower than 1503 and 1553. This could be attributed to an increased number of defects in the samples 1554 and 1555. To be precise, under the scope of the Arrhenius comparison, it seems that 1554, holds its relative intensity well, up until the point that the carriers are energetic enough to escape to the WL. From that point on, the intensity plummets, suggesting that the carriers in the WL have significant non-radiative recombination paths, in the form of crystal defects. The same happens to 1555. On the other hand, 1503 and 1553, whose relative intensities start dropping at lower temperatures, have comparable relative intensities with 1555 at room temperature, suggesting fewer defects.

Another result which interesting is that the activation energies of the samples extracted above, seem to be systematically off by a few tens of nanometers from the WL emission peak obtained from the PL spectra. This fact can be attributed to a Stokes shift of the WL emission line compared to the absorption peak. The shift is driven by fluctuations in the WL width and composition [29]. When excitons are thermalized to the WL, they lose energy by releasing phonons before relaxing to the potential energy minimum, where they decay. The PL peak corresponds to emission from the excitons, after they have relaxed to the potential energy minimum. On the other hand, the absorption peak extracted from the activation energy, corresponds to a statistical average of the energy needed for the exciton thermalization to WL, independent of width. If the WL width and composition were constant, the PL and the absorption peaks would coincide. However, due to random fluctuations, the WL width and composition are not constant, resulting in the Stokes shift. Based on the statistical nature of the activation energy, we can speculate that the Stokes



Sample	E_a (meV)	a	E_b (meV)	b	WL(nm)	FWHM(meV)	ΔE_{WL} (meV)
1503	64	180	165	$2 \cdot 10^5$	839	56	41
1553	46	46	179	$1.5 \cdot 10^5$	836	57	49
1554	32	8	235	$9 \cdot 10^6$	798	82	33
1555	83	358	260	$5 \cdot 10^6$	799	100	60

Figure 2.11: Top: Comparison between the samples of the chapter, indicating with arrows the corresponding WL peak extracted from the activation energy. Bottom: Table with the fitting constants of Eq.2.1 and the related quantities for each sample.

shift of the WL could be a measure of the density of the WL width fluctuations. The shift is found to be somewhat related to the full-width at half-maximum (FWHM) of the PL peak, shown in the table in Fig.2.11.

As a result, the difference between the PL peak and the peak corresponding to the activation energy could be a measure on the density of WL width fluctuations.

In this chapter we examined a core ingredient of high temperature single-photon emission, the short period super-lattice. Using simple simulations we were able to gather insight on the effect of the SSLs on the QD emission. A series of samples with different SSLs were grown and examined in order to find the most robust at high temperatures, while also having other characteristics that fit our needs, such as the emission range. It should be clear that this investigation is done exclusively for the purpose of high temperature emission. This is the reason why the samples were characterized only with macro-PL. In order to have emission of single-photons “on demand” we would need, of course, a single emitter, i.e a single dot. In order to study single dots, we need micro-PL characterization. However, when trying to do single-dot spectroscopy, one comes across the fact that the signal obtained is relatively weak. In order to enhance the detected signal, people have been using resonant structures like cavities [30], along with other more sophisticated structures such as photonic

wires [31]. Using the first approach, we embed the already investigated SSLs and the dots inside a cavity, with the ultimate goal being single-dot spectroscopy. This will be the topic of the next chapter.

Chapter 3

Quantum dots in a Cavity

As already mentioned in the motivation of this thesis, the core subject is to have single photon emitters operating at as much elevated temperatures as possible. The path towards having QD based optoelectronic devices inevitably crosses path with the coupling of the QDs with structures that enhance the signal. The approach we chose here is the use of a microcavity, a resonant structure, in which we will embed our QDs. The use of microcavities is convenient, because they are grown using molecular beam epitaxy (MBE), while we can use processing know-how already available in the Microelectronics Research Group (MRG) to create microcavity pillars, also called mesas, of diameters on the μm and submicron scale, to serve as signal enhancers. In this chapter, firstly we present some theoretical background on the influence of a planar cavity on the dot emission, as well as a coarse-grained model on how the microcavity pillar enhances the detected signal. Then follows an experimental investigation using macro-PL and reflectivity measurements to evaluate the samples. Finally, micro-PL measurements are performed on one of the samples, to obtain single-dot spectra and extract useful information, such as the strength of the signal, the exciton-biexciton splittings etc.

3.1 Theoretical Aspects

In this section, we will examine the theoretical basics of a QD inside a planar cavity, in order to shed light to the effect that the cavity has to the emission of the dots. Both theoretical implications and their consequence will be addressed.

To begin with, we will examine the problem at hand from a quantum optics stand point. The system of a photon emitter, such as the dot, an atom or any other small system, inside a cavity can be considered as special case to a more general concept. The general idea in question is the coupling of a small system to a large reservoir. In our case, the small system is a single quantum dot and the large reservoir is the photonic reservoir of a damped cavity, which is a cavity from which the photons are allowed to escape [32]. The combination could as well be an atom and the photonic reservoir or a QD coupled to both a photonic and a phononic reservoir. In any case, the treatment of the problem is more or less the same. Consider that the QD has two states, namely $|g\rangle$ which is the ground state and $|e\rangle$ which is the excited state. The excited state decays to the ground state with a rate of Γ_{QD} . The

cavity field has two states as well, which we will label as $|1\rangle$ for the excited, in which there is one photon inside. The ground state of the cavity field is labeled as $|0\rangle$, in which there are no photons. The cavity decays from the excited state to the ground state with a rate of Γ_c . In other words, the excited state of the dot has a lifetime of $\tau_{QD} \equiv 1/\Gamma_{QD}$, during which it emits a photon in the cavity and a photon in the cavity has a lifetime of $\tau_c \equiv 1/\Gamma_c$, during which it exits the cavity. A photon can be extinguished by either residual absorption in the cavity and photon scattering to cavity imperfections or by the transmission of the photon through the cavity boundaries. In our case, what is important are the photons transmitted through the cavity mirrors in order to be photo-detected, while the absorption and scattering are ignored in this discussion. Of course, a quantum dot does not have a single excited state, but we make this assumption in order to extract the basic physics that is important in this work, without making things too complicated. In this notation we can write the state of the system QD+cavity as:

$$|\Psi(t)\rangle = c_{e,0}|e, 0\rangle + c_{g,1}|g, 1\rangle, \quad (3.1)$$

where, for example, $|e, 0\rangle = |e\rangle \otimes |0\rangle$. In order to find the time evolution of the compound system we must solve the Schrödinger equation:

$$i\hbar \frac{\partial}{\partial t} |\Psi(t)\rangle = H_{eff} |\Psi(t)\rangle, \quad (3.2)$$

where H_{eff} is the effective Hamiltonian of the system. By effective Hamiltonian we mean the Hamiltonians of the composite systems plus terms which describe the decay of each system. The exact form and derivation of the Hamiltonian is out of the scope of this thesis, but both can be found in numerous quantum optics textbooks [33, 34]. In any case, the above equation must be solved in order to find the time evolution of the system.

At this point, some critical assumptions about our system must be made. The time evolution of the system changes drastically depending on the values of Γ_{QD} and Γ_c in relation to the coupling strength between the dot and the cavity. To be more specific, if the coupling of the dot with the cavity is comparable with the decay rates Γ_{QD} and Γ_c the system is in the so called strong coupling regime and undergoes damped Rabi oscillations. In other words, the photon has the probability to re-excite the dot before it exits the cavity. On the contrary, if the coupling strength is much smaller than Γ_{QD} and Γ_c the system is in the weak coupling regime in which it decays without any Rabi oscillations. The photon then exits the cavity as soon as it is emitted from the dot, assuming that $\Gamma_c > \Gamma_{QD}$.

In our case, the weak coupling conditions are well met. Assuming that the cavity has a single mode at wavelength λ_{cm} with linewidth $\Delta\lambda_{cm}$, the quality factor of the cavity is given by $Q_c = \lambda_{cm}/\Delta\lambda_{cm}$. The dot emits at wavelength λ_{QD} and has a linewidth of $\Delta\lambda_{QD}$. Because $\Delta\lambda_{QD}$ is small for quantum dots, typically sub-nanometer, and smaller than $\Delta\lambda_{cm}$, typically around 10 nm , the $\Gamma_c \gg \Gamma_{QD}$ condition is satisfied as well. In order to have a QD-cavity system in the strong coupling regime, one has to have cavities with high quality factors and small mode volumes [35]. Here, we use cavities with relatively small quality factors, for reason that will become clear later in the chapter, so we can safely say that we are in the weak coupling regime.

We are now ready to come back to our initial problem, what is the time evolution of the compound system, but under the assumption of weak coupling. By solving the Schrödinger

equation one finds a famous result, called the Purcell effect [36]: the decay rate of the QD is altered when the QD is inside the cavity. To be more specific, the decay rate of the dot is enhanced by a cavity contribution Γ'_c . The ratio between the contribution of the cavity and the decay rate of the dot in free space (with no cavity present), which is called the Purcell factor, is given by:

$$F_P \equiv \frac{\Gamma'_c}{\Gamma_{QD}} = Q \frac{6\pi}{Vk^3} = Q \frac{3\lambda^3}{4\pi^2 V n^3}. \quad (3.3)$$

The above equation shows that the two figures of merit defining the enhancement of the spontaneous decay rate are the quality factor Q and the cavity volume V . For more dominant Purcell effect, we need large quality factors, i.e. small $\Delta\lambda_{cm}$, and small cavity volumes in which the electromagnetic field will be confined.

Another way to reach to this result is to write the dot decay rate as:

$$\Gamma_{QD} = 2\pi \langle |g(\omega)|^2 \rangle \rho(\omega), \quad (3.4)$$

where $\rho(\omega)$ is the density of modes at frequency ω and $\langle |g(\omega)|^2 \rangle$ is the angular average of the coupling strength. In the case of a cavity, the density of modes is given by a Lorentzian centered at λ_{cm} . Assuming that the cavity is on resonance with the dot transition, the above equation is equal with equation (3.3). As one can imagine, equation (3.4), which is applicable to all kinds of systems, offers a tool to manipulate the decay rate of QDs. For example, one can chose structures with density of modes that suits his needs, such as photonic crystals, which exhibit a photonic band gap and spontaneous emission can be suppressed at certain wavelengths. [37, 38].

3.1.1 Signal Gain

In the previous paragraph, we considered the system of a dot inside the cavity and we described the basic physics that comes in play. The effects described were the consequences from inserting our emitter inside a resonant structure. As we saw, by doing that, we can modify the spontaneous emission rate, depending on the characteristics of the structure, in our case a cavity. So far, even though readily advertised, we have not yet discussed how the signal is enhanced. This paragraph is dedicated exactly to that. This crucial topic is pretty obscure and not well understood, but we will give a presentation of the related mechanisms and attempt to give a simple model of how the enhancement occurs.

To begin with, let us note that the increase to the signal translates to an increase to the number of photons detected. This can happen in two possible ways. The first is that the dot emission is increased, due to the Purcell effect described earlier. This increase is expected to have low impact on the total emission, since in our case we use relatively low Q factors, as explained in the next section, translating to Purcell factor of ~ 1.5 . The second possible way, which is the one that we believe plays the most important role, is the increase of the collection efficiency. The collection efficiency is the fraction of the signal collected to the total emitted radiation. In other words, the percentage of the emission that is collected is increased in the case where the dot is embedded inside a microcavity. This happens because, as explained below, in addition to the decay time of the QD, the radiation pattern is also modified in the presence of the cavity.

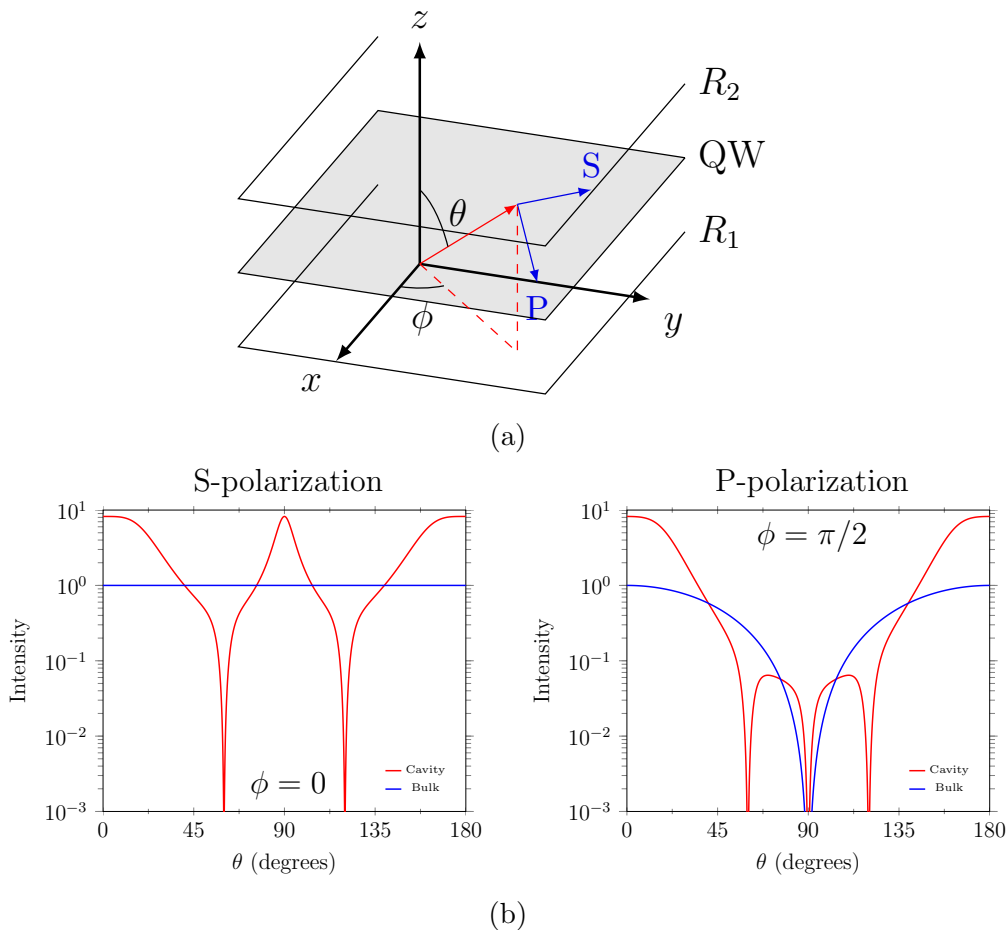


Figure 3.1: (a) Illustration of the model presented in the text, in which a QW is embedded inside a cavity. (b) The radiation intensity as a function of angle θ , with $\phi = 0$ for S-polarization (left) and $\phi = \pi/2$ for P-polarization (right), normalized for the free space value.

Before presenting the model, let us give some experimental parameters that will be taken in consideration. It is assumed that the radiation is collected with an objective lens with numerical aperture of 0.65. From equation $N.A. = n \sin \theta_{det}$, we get a maximum angle that can be detected of $\theta_{det} = 40^\circ$, for $n = 1$. Our capping layer is from GaAs, which has an index of refraction of ~ 3.6 , translating to a critical angle of $\sim 17^\circ$ and photons emitted at higher angles will be internally reflected. Using Snell's law, we see that rays with an incident angle greater than 10.3° , will have angles of refraction greater than 40° . In other words, only rays that are emitted in angles less than 10.3° compared to the perpendicular to the surface will be detected.

The calculation that follows, assumes a quantum well, the dipole moment of which lies on the xy plane with the z axis being normal to the cavity mirrors (Fig. 3.1a). The dipole is embedded in a planar cavity, the bottom mirror of which has a reflectivity of R_1 , while the top has a reflectivity of R_2 . The analysis assumes that the density of states is unchanged, but the vacuum field strength is modified, either enhanced or suppressed by the cavity. This seems to come in contrast to the previous paragraph, but it is actually the two sides

of the same coin. Because these quantities enter together, one can assume either one to be constant or variable. The radiation intensity, using spherical coordinates, at the point (r, θ, ϕ) is given by [39, 40]:

$$dI(r, \theta, \phi) = \frac{\eta P_{12}^2 E_0^0 (1 - R_2) \left[1 + R_1 - 2\sqrt{R_1} \cos(2kz_0 \cos\theta) \right]}{r^2 \left(1 - \sqrt{R_1 R_2} \right)^2 + 4\sqrt{R_1 R_2} \sin^2(kL \cos\theta)} \times \begin{cases} \cos^2 \phi, & \text{for S polarization} \\ \cos^2 \theta \sin^2 \phi, & \text{for P polarization} \end{cases},$$

where η is a constant, P_{12} is the dipole moment, E_0^0 is the vacuum field, k is the wavenumber, z_0 is the distance of the dipole from the bottom mirror and L is the cavity length. As we can see, the radiation pattern is modified and depends on the cavity characteristics. We will concentrate on a λ cavity, where the dipole is located in the middle, $L = \lambda$, $z_0 = \lambda/2$ or $kL = 2\pi$ and $kz_0 = \pi$. The reflectivities R_1 and R_2 used correspond to the reflectivities of a DBR stack with alternating GaAs and AlAs layers, with 14 and 4 periods respectively. Fig.3.1b shows the radiation pattern for the parameters above for the S and P polarization. As we can see, the radiation is primarily emitted at angles around 0° , 90° and 180° .

Next, we take four cases and we calculate the collection efficiency of each one, using the above model. The four cases are the following (Fig.3.2): a) a quantum well which is located in the planar cavity described above, b) a quantum well which is located inside the bulk of the semiconductor, corresponding to the case $R_1 = R_2 = 0$ in the above equation, c) a quantum well located in the same cavity as before, but it is now in a micro-pillar instead of planar, d) the same as the third case, but without the cavity. Generally, to calculate the intensity emitted we must integrate the above expression for the desired angles. In our model, the only differences between these four cases, are the angles that we have to consider in each case. To be more specific, in order to find the intensity collected through our objective for the cases that there is no cavity and no micro-pillar, where the photons exit through the top surface only, we have to consider angles less than $\theta = 10.3^\circ$ from the top surface. However, in the cases, where there is a cavity present, photons directed downwards at angles more than $\theta = 169.7^\circ$ will be reflected upwards, towards the objective, so they must be included as well. In the cases where the structure is not planar, we must take into account that there are photons exiting from the sidewalls at angles $73^\circ < \theta < 79.7^\circ$, that also make it in the collection path. The four cases and their corresponding collection efficiencies β are summarized in Fig.3.2. As we can see, the β for the first case is 0.223, for the second 0.012, for the third 0.232 and for the fourth 0.057. As we expected from the radiation pattern in Fig.3.1, the collection efficiency is increased when there is a cavity present compared to the case where there is not, due to redirection at small angles. In addition, in the cases where we have micro-pillars, the collection efficiency is increased slightly for the cavity case and more for the no cavity case. The collection efficiency with mesas, is increased further for the non cavity case, since the emission is isotropic and the percentage emitted from the sidewalls is relatively larger. Our results, showing similar β for the planar cavity and when the cavity

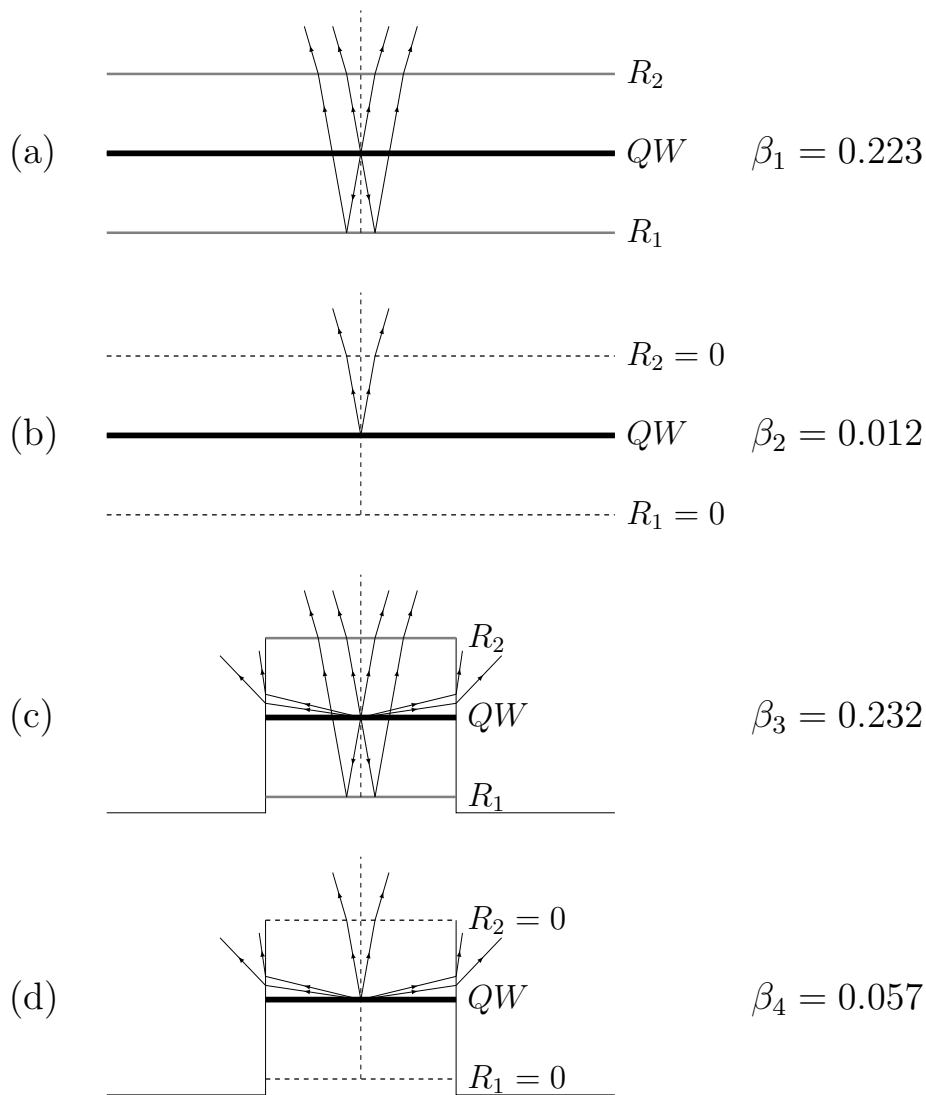


Figure 3.2: The four cases used for the calculation presented in the text and their corresponding collection efficiency.

is in a micro-pillar, suggest that we would get approximately the same signal enhancement either by creating mesas, or by simply opening nano-apertures on top of a planar cavity.

It is obvious that the calculation above makes several drastic assumptions about the system and we attempt now to address them and give some estimate on their influence. The first simplification done, is that the top and bottom mirrors are considered as metal mirrors with the same reflectivity of the top and bottom DBR respectively. However, the analysis is different when using DBR stacks and transfer matrices approach must be used [39, 40]. To be more specific, when the mirrors are from DBR stacks, a larger percentage of the emission occurs at larger angles, meaning that the radiation is more isotropic than the case examined here. As a result, we would expect that the collection efficiency would be higher for the case were the cavity is on a pillar, in contrast to the planar case. Another big assumption is considering a quantum well instead of a quantum dot. This is a major

simplification, but the basic physics is expected to be the same. Another assumption is that the depth of the QW from the surface is the same whether we have a cavity or not, which is not the case. When no cavity is present, the QDs are capped with only 100 nm of GaAs, compared to the ~ 600 nm thickness of the top DBR. Lastly, another arguable assumption is that we ignore any effect that the lateral confinement of the radiation field, has on the collection efficiency when we have micro-pillars, . This phenomenon has been shown to play a significant role in the increase of the coupling of the modes near “the fundamental mode”, or at angles $\theta \simeq 0^\circ$ [41]. To be more precise, the phenomenon of lateral confinement of the modes and the wave-guiding of the radiation towards the top surface, is the driving force behind the use of photonic nanowires, leading to enhanced collection efficiencies [42]. These photonic nanowires are non-resonant structures (without cavity) of micro-pillars where their diameter and height is tailored to enhance the collection efficiency through wave guiding. In our case, where we have a cavity inside a micro-pillar, but neither narrow nor long enough, we can expect to be affected by both of these phenomena. In other words, the radiation pattern is modified, leading to higher collection efficiencies, both because of the cavity effect and because some weak wave guiding occurring.

3.2 Experimental

In an attempt to do single dot spectroscopy experiments, one comes across the fact that the signal measured is relatively low, down to a few tens of counts per second (c.p.s.). As showed in the previous section, we must use a cavity in which the QDs will be incorporated. By using a cavity the measured signal is significantly increased, by up to 20 times, reaching a few hundreds counts per second.

In this scope we have grown a series of samples which are samples with InAs QDs embedded in SSLs inside a cavity. The samples in general have the same structure: a bottom stack of DBRs, a top stack of DBRs and the SSL-sandwiched QD layer in the middle. The DBRs are layers of GaAs and AlAs repeated for a number of periods, which are roughly one order of magnitude thicker than the layers for the SSL. The top stack is designed to have a much lower reflectivity than the bottom stack, so the photons escape the cavity from the top part, to the detector. Note that the SSL structure studied in the previous chapter is used in these samples, in order to achieve high temperature emission, so some of the samples presented there will be also used in this chapter.

The cavities used here are λ cavities and they are carefully designed to suit our needs [43]. One parameter we want to control when designing the cavity is the wavelength at which the cavity mode (λ_{cm}) appears. In principle, the cavity lets photons of wavelength λ_{cm} escape, while having a very high reflectivity for the other wavelengths, acting as a mirror. When designing the cavity, we want to place the cavity mode at the range of the quantum dot ensemble emission, in order to enhance it. Another parameter is the quality factor (Q) of the cavity designed. The quality factor, as mentioned earlier, is a measure of how sharp or broad the cavity mode will be. The quality factor is also a measure of how strongly a QD is coupled to the cavity structure.

Having in mind the high temperature emission from our dots, poses some restrictions on the above parameters. First of all, it is important to have in mind that the temperature

dependence is not identical for the quantum dot ensemble emission and the cavity mode. To be specific, the QD emission is expected to red-shift by $\sim 40 \text{ nm}$ as the temperature rises from 13K to room temperature, while the corresponding shift of the cavity mode is expected to be only $\sim 10 \text{ nm}$. As a result, the high temperature emission by QDs in a cavity is not a trivial task, as one would think, and the cavity mode must be placed wisely to ensure maximum output. For example, one can place λ_{cm} in the center of the QD emission. By doing that, we achieve an enhancement at low temperatures, but as the temperature rises, the QD emission will shift past the cavity mode. On the other hand, we can place the cavity mode in such a way, that the QD emission will shift on top of it at elevated temperatures. This was the motivation behind the choice of the 950 nm central wavelength at 200K , made in the previous chapter when extracting the activation energies of the SSL samples. In other words, we had in mind of a cavity mode centered at 950 nm and we wanted to see how the PL holds for the quantum dots that would emit at $\sim \lambda_{cm}$ at 200K .

Another parameter taken into account, when designing a cavity for high temperature emission is the quality factor Q . In the theoretical section of this chapter, we saw that in order to have significant Purcell effect we must have large quality factors. However, the quality factors chosen for the cavities in this chapter, are rather small. The reason behind this is that we want the emission to be enhanced for a significant range of temperatures, which is convenient when examining emission from single dots. Another benefit of small quality factors is that both the exciton and the biexciton line of the same dot are enhanced, necessary to be able to perform cross-correlation experiments, which are essential for entanglement measurements.

In order to achieve the desired values for Q and cavity mode wavelength, we must carefully chose the number of periods of the bottom and top DBRs, as well as the cavity length, i.e the number of periods of the SSLs. The structure was modeled in previous works by a code using transfer matrices [44], that extracts the relevant quantities. The growth of the samples is similar to the growth of the SSL samples, presented in the experimental part of the previous chapter. The only difference is the growth of the DBRs that sandwiches the SSLs and the dots. The growth for the AlAs and GaAs layers in the DBR takes place at around 635°C and the SSL is grown at the same temperature. Following the SSL, the dots are grown, with conditions that will be given for each sample separately. Then, the top SSL is grown and the temperature gradually rises back to 635°C in the first 10 SSL periods, and stays there for the rest of the SSL, as well as the top DBR stack. The temperature ramp is necessary because the aluminum atoms need higher temperature to find their lattice positions in the thick AlAs layer of the DBR, but the indium atoms desorb heavily at high temperatures. As a result, the solution of gradual temperature increase is chosen.

The PL characterization is done exactly as described in the previous chapter, with the only difference being the use of a 655 nm diode laser, in addition to the 325 nm He-Cd laser used before. The reason behind this, is that the top DBR is rather thick and photons with higher wavelength have higher penetration depth to photo-excite carriers at the depth where the QDs exist. The reflectivity of the samples is now measured as well, in order to identify the cavity characteristics. For this we use a halogen lamp coupled to an optic fiber. The light is guided perpendicular to a reference mirror first and the reflected light is guided back to the spectrograph. Then, the same is repeated for the sample and the reflectivity

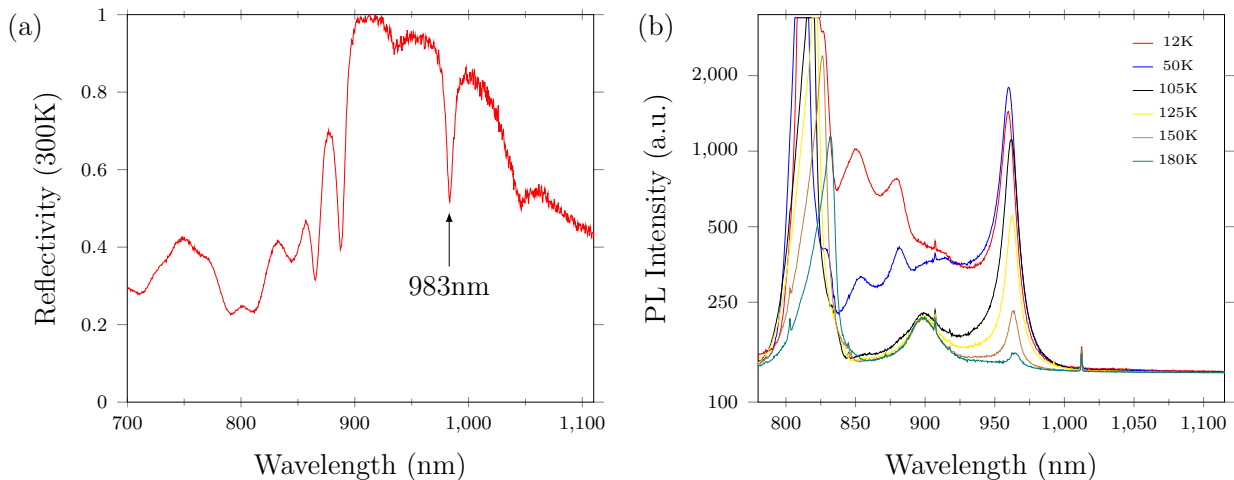


Figure 3.3: (a) The room temperature reflectivity of sample 1508, the cavity mode is centered at 983 nm and the quality factor is 136. (b) The low temperature PL, which shows a peak at 960 nm , corresponding to emission from dots that emit at the cavity mode.

is calculated as the ratio of the light reflected from the sample to that reflected from the mirror. It is important to note that the reflectivity obtained is still not the absolute value, due to the fact that the reflectivity of the sample is measured with the sample on top of the mirror and thus at different distances from the fiber. For the absolute value, we would have to measure both at the same distance.

For the purposes of this topic a total of nine samples were grown. Here we choose to show only three of these samples, the ones which were the most successful. The growth of the cavity samples is more demanding, due to the relatively thick DBRs, so there are more points where it can go wrong. In other words, the cavity samples pose bigger growth challenges and as a result, the structure may not have the desired cavity characteristics or may not have intense QD emission.

3.2.1 Sample 1508

The first sample is labeled 1508. It is grown on a semi-insulating substrate and the cavity consists of the bottom DBR of 67.8 nm GaAs followed by 79.3 nm AlAs, repeated for 14 periods. Next follows the SSL of 16 \AA AlAs and 12 \AA GaAs repeated for 52 periods. The quantum dots are grown at a temperature of $T_g = 450^\circ\text{C}$, a growth duration of $t_t = 18\text{ sec}$ and a growth rate of 0.1 ML/sec . Then, a top SSL of 55 periods of 12 \AA GaAs and 16 \AA AlAs follows right after and finally, the top stack of DBR of 79.3 nm AlAs followed by 67.8 nm GaAs, which is repeated for 4 periods. In short, the sample has the SSL structure and QD growth conditions of 1503 and could be considered as 1503 embedded in the cavity specified above. The cavity is designed to have the cavity mode at 950 nm . In Fig. 3.3a we can see the reflectivity obtained for 1508 at room temperature. The cavity mode is centered at $\sim 983\text{ nm}$ and the quality factor is 120. The PL of the sample is shown in Fig. 3.3b. The peak centered at 960 nm , at low temperature, corresponds to the QD emission filtered by the cavity mode. It is shifted compared to the cavity mode wavelength seen in the reflectivity

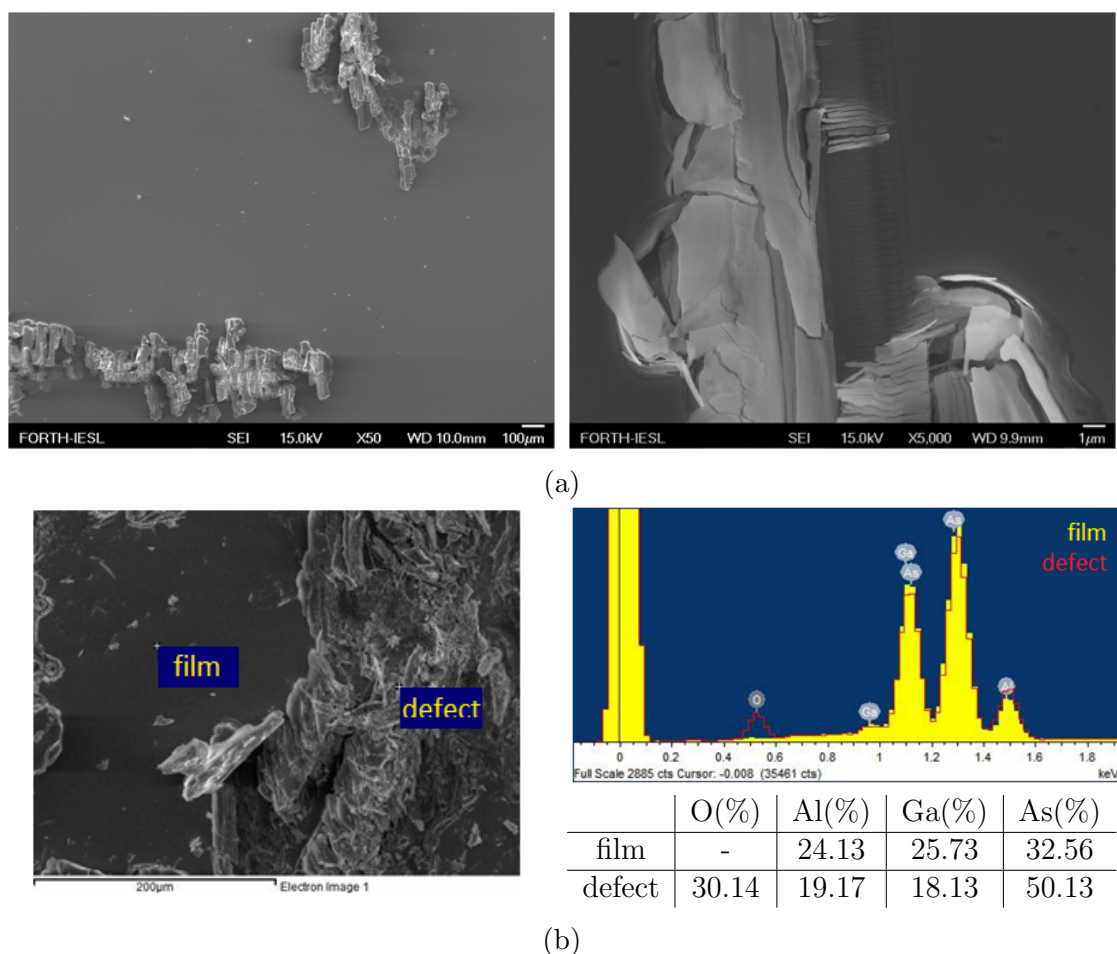


Figure 3.4: (a) Images from SEM of 1508, from an area with surface degradation. (b) The EDX study performed on degraded and non-degraded areas of 1508.

partly due to the different temperature of the measurements, and possibly due to sample inhomogeneity. However, the QD peak resembles the cavity mode. As we can see, as the temperature rises the QD emission is quenched at around 180K, even though sample 1503 showed emission up to room temperature. This is because now, as the temperature rises, not only the dots lose carriers to the WL, but fewer and fewer dots emit at the cavity mode, due to the shift of the emission past the cavity mode wavelength. The broad and intense emission at $\sim 815 \text{ nm}$, which is saturated, corresponds to emission from GaAs present in the DBRs.

3.2.2 Surface Degradation

Later, when deciding which sample to do micro-PL on and after examining the sample, we came across the fact that areas of the surface of the sample were altered. To be more specific, the surface had become rougher on several spots, with different coloring than the rest of the surface. During the cavity samples investigation, the same effect appeared on all the samples. This surface degradation seems to be happening in about a few weeks after the

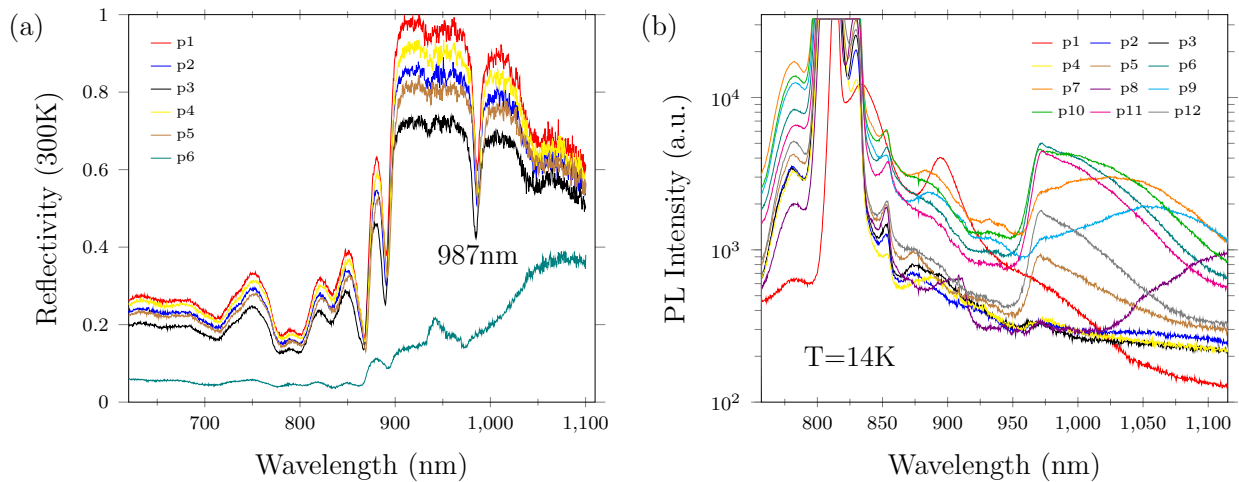


Figure 3.5: (a) The room temperature reflectivity mapping of 1508, after the surface degradation has taken place. We can see that only one spot was significantly damaged. (b) The corresponding low temperature PL, showing a heavily distorted emission compared to the first PL measurement of the sample.

sample growth, in similar extent to all the samples. A scanning electron-beam microscopy (SEM) and an energy-dispersive X-ray spectroscopy (EDX) study has been carried to figure out the structure and composition in the degraded areas. The results are shown in Fig. 3.4. As we can see in the composition of the defect obtained from EDX, there is significant oxygen content ($\sim 30\%$) in the degraded areas, suggesting some kind of oxidation. In contrast, the aluminum, the gallium and the arsenic is slightly reduced, compared to the “healthy” areas. However, the damage on the sample is not limited to the surface only. This can be seen when measuring the reflectivity and the PL of 1508, after the surface was degraded, as shown in Fig. 3.5, for different areas of the sample. Note that the reflectivity is not changed much for most of the areas measured, except for a 4nm red-shift of the cavity mode. The PL, on the other hand, is heavily disturbed, suggesting that the phenomenon affects more drastically the QD emission. The cause of this is not clear. One possible explanation could be defects, such as dislocations, that propagate through the sample, all the way to the surface. As a result, aluminum could potentially make its way to surface, causing some sort of oxidation. Another more probable explanation is that oxygen penetrates deep into the structure, causing the oxidation at a greater depth and spreads from within to the surface. It should be noted that this effect is more prominent in high index substrates, compared to (100). In any case, one way to protect these samples from degradation, is to put them in an oxygen-free environment with constant nitrogen flux. Also, as we found out, the processing of the sample for micro-PL measurements, i.e the formation of micro-pillars by reactive-ion etching (RIE), seems to halt the degradation mechanism. As a result, in order to perform micro-PL on a cavity sample, we found out that immediate processing is required. Thus, once a sample is characterized and evaluated to be studied in micro-PL, the processing must be done as soon as possible to limit any degradation.

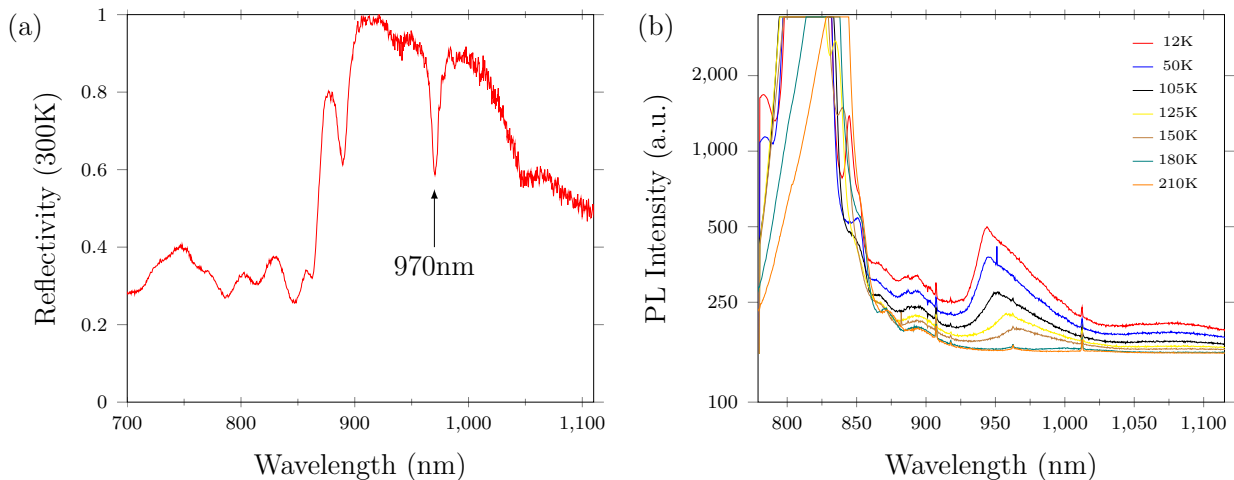


Figure 3.6: (a) The reflectivity measured for 1509, the cavity of which has a quality factor $Q = 136$ and the cavity mode at $\lambda_{cm} = 970 \text{ nm}$. (b) The PL measured for 1509, showing a relatively broad dot emission, which is not characteristic emission of QDs inside a cavity.

3.2.3 Sample 1509

The next sample of the series is labeled as 1509. The structure is the same as 1508, with the only difference being the reduction in the cavity length. The DBR stack thickness and periods are same, as well as the dot growth conditions, but the cavity length is reduced by reducing the SSL periods from 52 to 48. This change is done in order to shift the cavity mode closer to the 950 nm mark, for the reasons explained earlier. The reflectivity of the sample is shown in Fig.3.6a. The cavity mode has indeed shifted, to $\sim 970 \text{ nm}$ and the quality factor is now 136. The PL of the sample is shown in Fig.3.6b and we can see that the dot emission is present and is rather broad, in contrast to 1508 that had a well-defined peak, which does not exactly follow the cavity mode as seen in the reflectivity of the sample. The cause of this is not certain, but a possible explanation, based on the resemblance of the 1509 PL to the 1508 PL after the surface degradation, is that the sample was already damaged to some extent at the time of the measurement.

3.2.4 Sample 1572

Following the growth of a number of cavity samples, which did not work as intended, either by having the cavity mode off or by not showing PL even when the cavity mode was correctly placed, we decided to use the new QD growth conditions used in samples 1553, 1554 and 1555. Out of these three, we chose to go with sample 1553, for which the SSL layer thicknesses are the same as 1508 and 1509, with the only difference being the use of 1553 QD growth conditions, instead of the conditions of 1503 used in 1508 and 1509. The reason behind the selection of 1553 instead of 1554 and 1555, is that it has strong emission and it seems to hold better as the temperature increases than the rest. However, by changing from 1503 to 1553 growth conditions we increase the QD density, so this may pose a problem when trying to do single-dot spectroscopy. In any case, the number of SSL periods is now

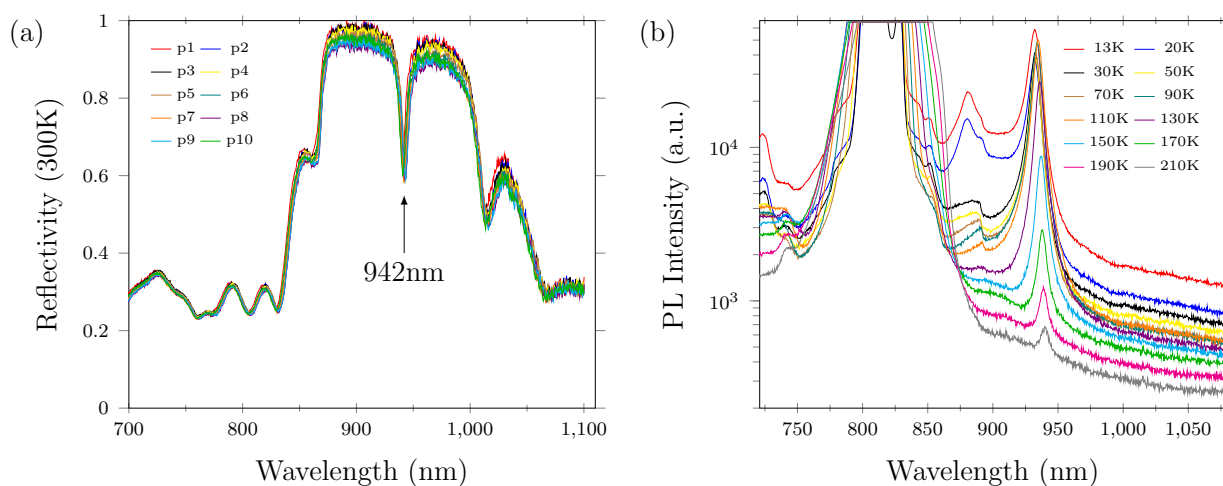


Figure 3.7: (a) The reflectivity mapping of sample 1572, showing a cavity with very few fluctuations across the sample. The cavity mode is centered at 942 nm and the quality factor is 154. (b) The PL of the sample, showing strong a QD emission peak at 932 nm , for low temperatures.

reduced to 44 and the reflectivity of the sample is shown in Fig. 3.7a. As we can see, the cavity mode is centered at $\sim 942\text{ nm}$ and the quality factor is ~ 154 . The PL is shown in Fig. 3.7b, where we can see a peak corresponding to the QD emission. The intensity of the sample is stronger than the intensity of the two previous samples by a factor of ~ 20 . As expected, the change on the QD growth conditions, which resulted in an intensity increase from sample 1503 to 1553 by a factor of 2, is reflected also when we embed our dots inside a cavity. Taking into account that the sample has the cavity mode at the wavelength that it was designed to be and that it shows strong dot emission in the cavity mode, we decided to further study it by performing micro-PL experiments. For this purpose, after the initial measurements, the sample was given for processing to ensure that surface degradation is limited.

3.2.5 micro-PL

The last part of this chapter is dedicated to the micro-PL measurements performed on sample 1572. These measurements serve as an investigation on the single-QD emission characteristics of the sample. To be precise, the scope of this investigation is to point out possible candidate quantum dots, on which single-photon measurements will be performed and to extract general tendencies of the sample, such as the intensity of the QD emission, the excitonic linewidth and the exciton-biexciton splittings.

Before presenting the experimental setup and the results, we will briefly mention the process flow for the fabrication of micro-pillars, or also called mesas, on the sample. These micro-pillars serve as markers on the surface, convenient for reproducible mapping of the sample. They could also serve as some sort of wave-guides, provided that their diameter was sufficiently small and their height sufficiently large [45]. The patterning process is the following. First, the indium from the backside of the sample is removed by polishing the backside by lapping. This indium is used for the mounting of the substrate on the molybdenum block

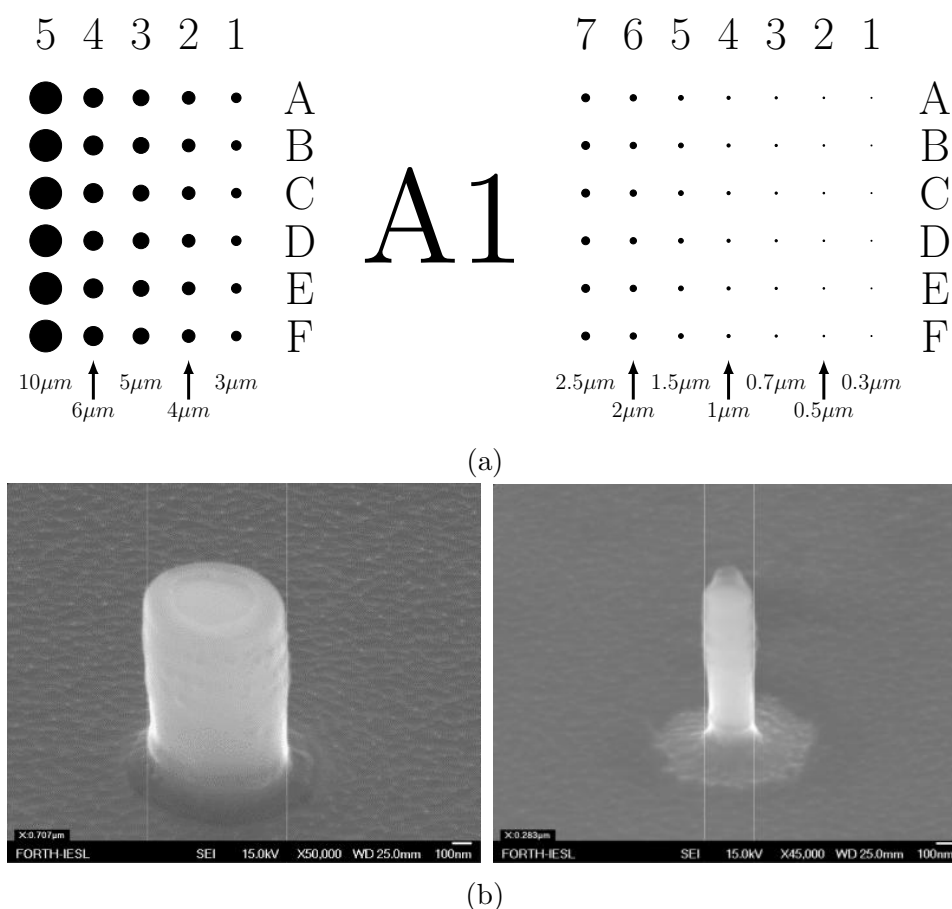


Figure 3.8: (a) The layout of one period of the pattern formed by electron-beam lithography of the surface of the sample. A total of 100 periods in a square mesh, are created. (b) The mesas formed by reactive ion etching, their diameter ranges from $10 \mu\text{m}$ to $0.3 \mu\text{m}$. Their sidewalls are vertical and their depth is such that the etching front is inside the bottom DBR.

inside the growth chamber. Then, after indium removal, a suitable polymer, used as a mask, is deposited by spin coating. The wanted pattern is generated by electron-beam lithography and one period of the design layout with the corresponding dimensions is shown in Fig.3.8a. A total of 100 periods like the one shown are created. Then, the resist is removed from the areas of the surface not exposed to the electron-beam, leaving the sample surface uncovered, and the only resist left is on the exposed areas, i.e. on the wanted patterns, serving as a protective mask for the formation of micro-pillars using reactive ion etching. The reactive ion etching (RIE) is required because of the anisotropic etching needed for the formation of vertical sidewalls of the micro-pillars. The etching depth depends on the structure of the sample. For the microcavity samples, the depth is about $0.6 \mu\text{m}$ and gets in the bottom DBR stack by 2-3 periods. Finally, after the micro-pillar formation, the polymer is removed by standard degreasing, using acetone, isopropanol, and deionized water. The final product is shown in Fig.3.8b, showing well formed mesas with relatively smooth vertical sidewalls.

After the macro-PL characterization and the micro-pillar formation by the process flow described above, the sample is ready for micro-PL measurements. The sources for the

QD excitation used are a continuous wave (CW) diode laser at 532 nm and later a mode locked tunable Ti:Sapphire laser, with repetition rate 76MHz and pulse duration of $\sim 80\text{ fs}$, tuned at 770 nm . For the latter case, a spatial filtering setup was used to create a clean Gaussian beam profile to control its shape. The sample is held on a continuous flow liquid nitrogen cooled cryostat, capable of temperatures down to 77K . The vacuum of the chamber is at around 10^{-5} mbar . The beam is focused on the sample using a $40\times$ objective with a numerical aperture of 0.65 , translating to spatial resolution of about $1 - 2\ \mu\text{m}$. The power of the laser focused on the sample is controlled using a continuously variable neutral density filter wheel, ranging from ND0 to ND4. The micro-PL signal from the dots is collected from the same objective and is analyzed through a 0.75m spectrograph, which has a 1200 gr/mm grating, blazed at 750nm . The analyzed spectra are recorded using a high quantum efficiency back-thinned liquid nitrogen-cooled CCD.

It is important to note the reason behind the use of two different lasers as excitation sources. At first we used only the CW diode laser, but later we chose to use the Ti:Sapphire as well. The most significant difference between the two lasers is their wavelength, the first being at 532 nm and the second being locked at 770 nm . The wavelength of the laser determines the penetration depth, but most importantly it determines the region where the carrier excitation takes place. To be more specific, recalling the simulation results from Chapter 2 (Fig. 2.1), the SSL of sample 1572 is expected to have a direct band gap at around 590 nm . As a result, when the excitation source has a wavelength lower than 590 nm , carriers can be excited in the SSL. Then, they are relaxed into the WL and finally to the QD, by the emission of phonons. Considering that, while relaxing to the QD, the carriers may get trapped to defects, creating localized charges and thus affecting the dot emission, we later decided to use the second laser at 770 nm . At this wavelength, the laser cannot excite carriers in the SSL, but pumps the dots via the WL which emits at 817 nm in these QDs. As a result, we avoid excitation in the SSL region, where the AlAs is more prone to defects compared to GaAs. For the excitation, we could also use quasi-resonant and resonant conditions. In other words, we could tune the laser to be on resonance with excited states or the ground state of the dot, called quasi-resonant and resonant excitation conditions respectively. However, experiments where the emission is close to the laser are more difficult to implement.

The first results we would like to present is the difference between the two excitation sources on single mesas. Note that in the spectra presented here, only mesas with diameter 300 nm are taken in consideration. This is because based on the QD density of the sample, which is the same as 1553, an average of 6 dots is expected in the mesa of diameter 300 nm . As a result, since this number is already high for single dot spectroscopy, we investigated only the mesas of the smallest diameter. The results of two different mesas for the two different lasers are shown in Fig.3.9. The mesas chosen, show both a large number of dots (a) and a fewer number (b). The lines correspond to excitonic and biexcitonic states of the QDs in the mesa. As we can see, the dots need higher power when excited with 770 nm to exhibit the same intensity as when excited with 532 nm . This is because, when using 532 nm we excite carriers in the SSL, where as with 770 nm we don't. As a result, we need more power to excite the same amount of carriers. However, above a certain power, where there are many carriers available, the emission is limited by the dot decay rate and the intensities

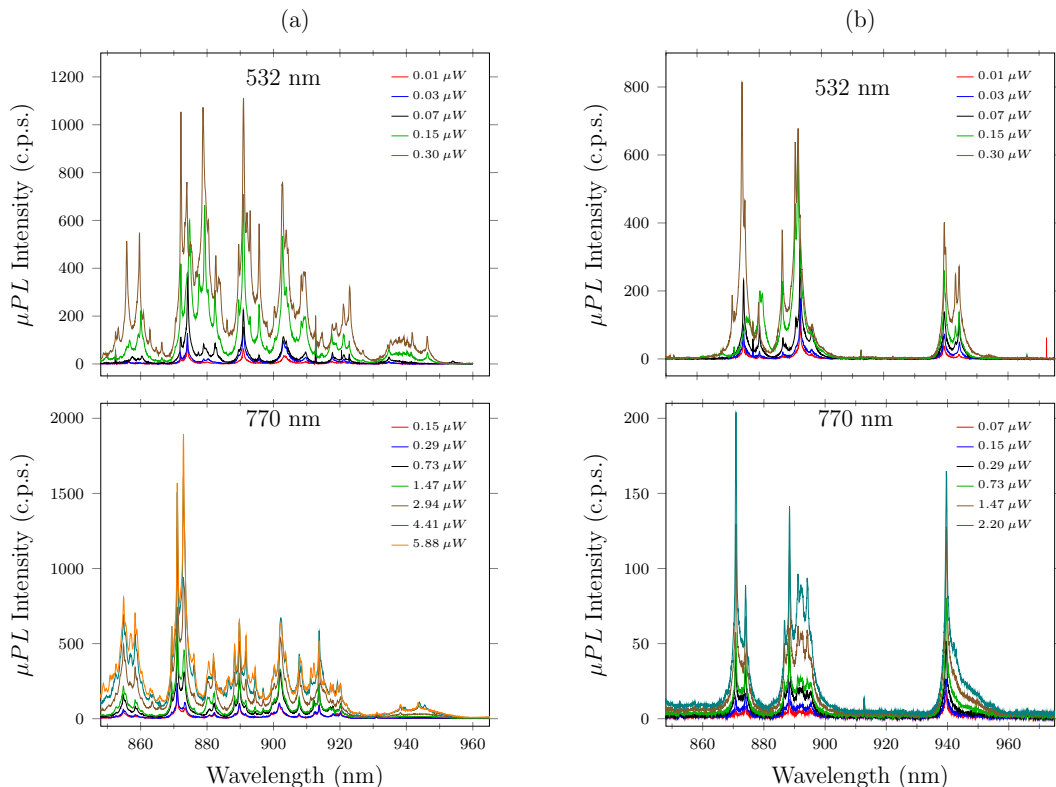


Figure 3.9: The micro-PL spectra of two different mesas, using 532 nm and 770 nm excitation wavelengths with increasing power of excitation.

are expected to be more or less constant and similar for both lasers. This is called saturation of the lines and the power value for the saturation depends on the dot, based on how easily it is “filled” with carriers. Another fact deduced from Fig.3.9 is that the lines from the 770 nm laser are a few nanometers blue-shifted compared to 532 nm. Since the cryostat was opened and the sample was re-mounted between the two measurements, we can assume that the sample in the first case was not properly mounted, and the temperature was a bit higher than 77K. As a result, in the following spectra mostly results from 770 nm excitation will be shown.

These results are shown in Fig.3.10, where we plot the micro-PL spectra for three different mesas using for excitation the 770 nm laser and one with the 532 nm laser. Here we will discuss the general traits of the sample based on the total of spectra obtained. First of all, as mentioned earlier, the sample has relatively high QD density and as a result, the mesas with a QD number of 2-3 are not a common occurrence. In general, the sample seems to have high intensity excitonic lines, ranging from 100-2000 c.p.s., comparable or even higher than samples studied previously. A peculiar trend which occurs is that the excitonic lines range from 850 nm to 960 nm when the 532 nm laser is used, while when the 7700 nm laser is used, the number of lines at wavelengths higher than 930 nm is reduced considerably. In general, the spectra with 770nm seem to be less “messier”, with more well-defined peaks and less noisy signal. We would also like to point out that with 532 nm, lines with intensities as high as 6000 c.p.s. have been measured, but because these intensities could not be

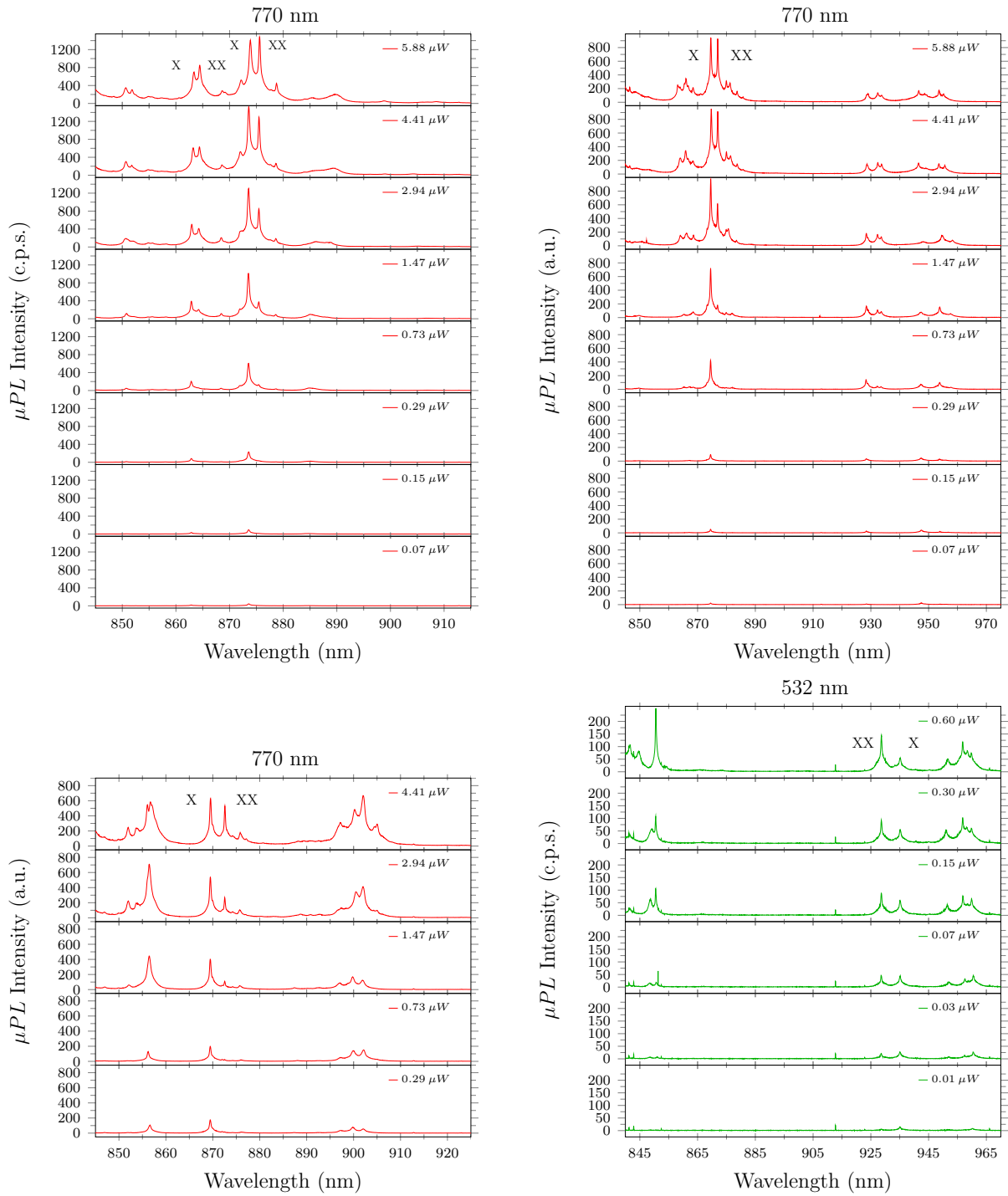


Figure 3.10: The micro-PL spectra for three different mesas for 770 nm and one for 532 nm. The spectra show exciton-biexciton pairs, as hinted by their power dependence.

repeated with 770 nm , we chose not to include them. Another characteristic of the excitonic lines is their relatively large linewidth. To be precise, the average linewidth of the lines is $\sim 1.5\text{ meV}$, while in previous samples the linewidth was below $\sim 1\text{ meV}$. In some cases, the lines also show significant spectral diffusion [46], i.e instances where the line wavelength seems to drift a few nanometers in the order of less than a second. Additionally, in some cases, there is significant blinking, where the emission seems to turn off and on. Both of the above phenomena are linked to the presence of charged sites in the vicinity of the dot, influencing dynamically the energy states of carriers inside the QD and the recombination of the exciton [47, 48]. The micro-PL measurement of the mesas where the above phenomena are intense is troublesome. The spectral diffusion and the blinking of the lines are power dependent, increasing as power increases, and also seem to be less present when the 770 nm laser is used as excitation source. Another interesting fact is that the sample seems to have both binding and anti-binding biexciton energies, as shown in Fig.3.10. However, this needs further investigation in order to be a concrete result. More thorough power dependent measurements must be done for each supposed exciton-biexciton pair, since the exciton must obey a linear power dependence, whereas the biexciton should obey a quadratic dependence on power. It is important to note that at saturation the biexciton intensity should be similar to the exciton intensity in the case of a pulsed excitation sources, contrary to a CW source where it can surpass it. This happens because, in the CW case the dot is continuously injected with carriers and as a result the biexciton recombination is only limited by its lifetime. On the other hand, in the case of a pulsed excitation, the carriers are injected in one pulse and they recombine before the next pulse. As a result, the number of carriers injected depends on the number of photons in the pulse, which is in other words the power of the laser. The X-XX energy difference from the exciton and biexciton lines seems to range from $\sim |3\text{ meV}|$ to $\sim |9\text{ meV}|$. These values are comparable to the values from earlier samples.

Something that would seem quite bizarre at first sight is that Fig.3.10 and the exciton emission range of $840\text{--}960\text{ nm}$ mentioned earlier, seem to be inconsistent with the macro-PL spectra shown in Fig.3.7. There, a peak which we attributed to QD emission was centered at 932 nm . On the other hand, the micro-PL results indicate that the emission is spread out significantly. To give some perspective, in Fig.3.11 we have plotted the intensity of excitonic lines versus wavelength and in the same plot we also depict the reflectivity response and the macro-PL of the sample. As we can see, the micro-PL emission is much more intense compared to QD emission without cavity structure (based on previously studied samples), but it seems to be blue-shifted by tens of nanometers from the macro-PL peak. The reason for this seemingly unjustified phenomenon lies on the micro-pillar structure used. To be more specific, the measurements of the reflectivity and the macro-PL correspond to the planar structure. However, the picture changes drastically when the structure is on micro-pillars with sub-micro diameters. The cavity is no longer planar and its photonic behavior is affected by the micro-pillar geometry. In other words, the cavity characteristics, such as the cavity mode wavelength and the quality factor, are different for each individual mesa. The cavity characteristics now depend on the mesa characteristics such as its diameter, any diameter fluctuations that may be present, the roughness of the sidewalls, etc. The quality factor is expected to decrease (more shallow cavity mode), since only 2-3 DBR periods exist

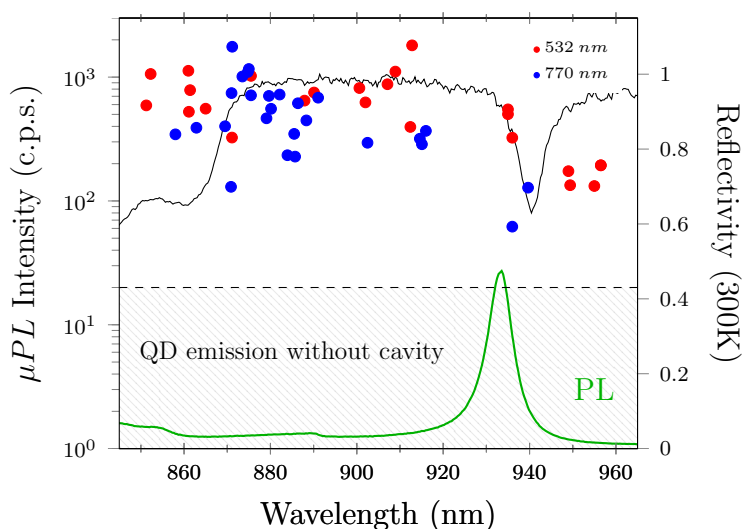


Figure 3.11: The emission lines from quantum dots from several different mesas, for both 532 nm and 770 nm wavelength of the excitation laser, compared to the reflectivity of the sample and the corresponding macro-PL, in addition to the QD emission intensity when no cavity is present.

in the mesa, with the rest in the bulk of the material. In any case, the macro-PL gives us a rough estimate of the sample emission, but when micro-pillars are formed for micro-PL measurements, the structure at hand differs from one mesa to the other.

In this chapter we examined the effect of embedding our quantum dots in a cavity. First, the theoretical background of a dot inside a planar cavity was given and a simple model on how the detected signal is amplified by the presence of a planar cavity and cavity inside a micro-pillar. Then, the three most successful samples of this series were presented and the surface degradation, a common occurrence on all cavity samples, was examined. Lastly, the micro-PL measurements performed were shown, in addition to the process flow of the micro-pillar formation. The micro-PL characterization revealed intense QD emission, compared to the QD emission when no cavity is present (3.10). It is important to note that the micro-PL measurements shown here are an investigation on the characteristics of the single-dot emission. They are preliminary measurements that will be used in anti-bunching and temperature dependent experiments, necessary for high temperature single photon emitters.

Chapter 4

Quantum dot capping with Aluminum Arsenide

In the final chapter of this thesis, we turn our attention on a different direction. Until now, we have focused on high temperature emission using the SSL and on the enhancement of the detected signal by using a cavity. Here, we focus on a new direction, not explored much in the literature as of yet. This chapter should be viewed as a side project of the work presented in the previous chapters. At first, the idea will be presented and afterwards the experimental results will be given.

The motivation behind the idea of this chapter stems from the results of Reference [19]. There, the QD strain profile has been deduced using HR-TEM and the indium chemical composition has been extracted using Vegard's law [49]. The results show an indium composition gradient from the base to the apex of the dots. To be more specific, the dots have low indium content, of ~ 0.3 just over the WL which increases towards the apex to ~ 0.74 . The indium chemical composition gradient appears only on the growth direction and not on the lateral dimensions. This result, which suggests that our dots are in fact a graded $\text{In}_x\text{Ga}_{1-x}\text{As}$ alloy, with varying x along the growth direction, is somewhat bothersome because the low indium chemical composition means that the internal piezoelectric field is much lower than the 0.8 MV/cm predicted for the pure (211) InAs dots [50]. As mentioned in the first chapter, the piezoelectric field is related to the FSS values and as a result we would want it to be as high as possible. The idea explored in this chapter is to increase the indium content by capping the dots in AlAs.

Before we go into some more detail about how AlAs capping may influence the dots, let us discuss briefly the mechanism related to the increased gallium content in the QDs. The mechanism is called surface segregation and it can be generally described as the phenomenon where the composition profile of a semiconductor alloy near the surface is different from the composition in the bulk. In III-V ternary alloys, like $\text{In}_x\text{Ga}_{1-x}\text{As}$, an enrichment of one of the third-column materials has been found to occur [51]. Generally, the driving force behind surface segregation is debated. In the literature we can find models based on both equilibrium thermodynamics and on non-equilibrium kinetic effects. In the first approach, when the system is in thermodynamic equilibrium, its free energy is minimal when the chemical potentials of indium and gallium atoms forming the bulk and the surface are

balanced out [52]. The material can minimize its free energy by having the alloy species that has the weakest bonds concentrate on the surface. Also in lattice-mismatched alloys the low-concentration species will be driven to the surface by 'strain release' because they experience less strain energy at the surface than in the bulk [53]. The other approach is a phenomenological kinetic description in which a certain fraction of indium atoms of the top surface layer segregate to the next layer, while the rest are incorporated into the bulk of the material, before the next monolayer is completed [54]. The fact that surface segregation depends strongly on the growth conditions, such as the growth temperature, the strain in the epitaxial layer, the growth rate, the type of the substrate, makes it difficult to give a clear description of the segregation phenomena. In the literature, a number of publications explore surface segregation on InAs/GaAs heterostructures, focusing on the dependence to the growth conditions of quantum wells [54, 55], quantum dots [56, 52] and in general the GaAs/InAs interface [57, 58].

We now turn our attention to the main feature of this chapter, which is the capping of the dots by a thin AlAs layer. There are reports showing that by using AlAs as a capping layer directly on top of the dots, before the GaAs capping layer, the surface segregation is reduced and the indium content is increased. To be more precise, the AlAs layer cap has been shown to redshift the QD emission, consistent with the higher indium content, while also not affecting the QD density [59]. In contrast, the dots were found to be more uniform when capped with up to 3ML AlAs. As expected, the phenomenon was found to be temperature dependent, with the segregation being reduced more for higher substrate temperatures. Similar results were found in [60]. There, the red-shift of the emission from a stacked structure of InAs QDs was reported, when an AlAs capping layer as thin as 0.2ML was inserted right before and right after the dots. The redshift of the QD emission by a 10ML AlAs capping layer was also reported in [61]. There, they also found that the relatively thick ,compared to the two references above, AlAs also caused a "double peak" PL spectrum, which they attributed to two different QD families, based on their height compared to the AlAs layer. It should be noted that in all of the above publications, they worked on quantum dots grown on (100) substrates. To our knowledge, no publication exists for the effect of AlAs capping on QDs grown on the (211) crystallographic orientation, as of yet.

4.1 Experimental

Based on the reports described above, we decided to investigate the concept of capping our dots with AlAs, in order to obtain higher indium content in them. As one can deduce from the brief description given above of prior work done on the subject, it is not clear how much AlAs should be deposited on the dots. The thickness of the AlAs capping layer varies between 0.08ML to 10ML depending of the reference, a significant disparity. Also, because the effect seems to be strongly dependent on the growth temperature we decided to investigate the effect that the AlAs capping layer has on dots, using typical growth conditions, the same used in the samples of the previous chapter, with a starting point of 1ML AlAs. The effect of AlAs capping was investigated both by PL characterization to find out how the emission changes and AFM characterization, in order to extract how the QD

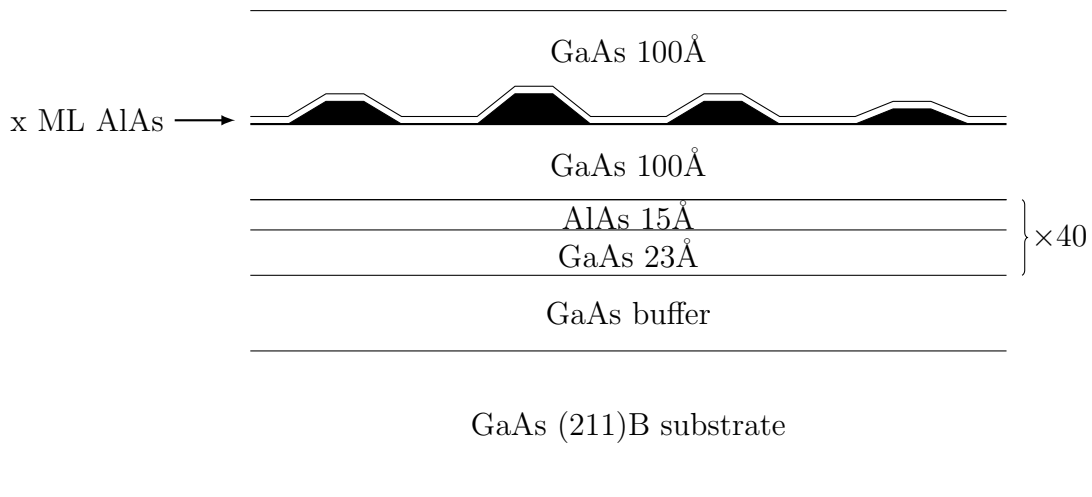


Figure 4.1: The structure of the samples used for the AlAs capping investigation. The value of x varies between each sample.

characteristics, such as diameter, height and density, are affected.

The growth of the samples is performed as described in previous chapters. After the removal of the native oxide by thermal annealing, a GaAs buffer layer is grown. Then, follows a 40 period SSL (23 Å GaAs, 16 Å AlAs) grown at 600°C and afterwards a 10 nm thick GaAs layer, on which the dots are formed. The growth conditions of the dots are the same for all the samples in this chapter. The growth temperature is set at 480°C, the growth duration is 18 sec and the growth rate 0.1ML/s. The AlAs capping layer is grown on top of the dots at the same temperature. Finally, the sample is capped with a 10 nm GaAs layer. A schematic illustration of the structure is shown in Fig.4.1. It is important to note here that the substrate used in the first samples was n^+ type, but later a semi-insulating substrate is used, for reasons explained later. For the optical characterization, the PL setup described in the previous chapters was used. The excitation source is the He:Cd laser emitting at 325 nm. The details of the setup are presented in Chapter 2.

4.1.1 Reference Samples

In the investigation of capping our dots with AlAs, it is important to have reference samples, with no AlAs capping, with which we will compare the samples with AlAs. For this reason, the reference samples 1540 and 1541 were grown. The substrate used was of the n^+ type. The first is an uncapped sample, meaning that the top GaAs cap is not present. After sample 1540 was grown, 1541 was grown on a second holder with the GaAs capping. In general, the samples on which AFM characterization is taking place, are left uncapped, while samples with the GaAs capping are characterized by photo-luminescence. The AFM results are shown in Fig.4.2a. The average height of the dots is 2 – 3 nm and their average diameter about 40 nm, while their density is $\sim 2 \cdot 10^{10} \text{ cm}^{-2}$. Notice the presence of a few larger dots, showing elongation along one dimension, with height $\sim 15 \text{ nm}$ and large base diameter of $\sim 100 \text{ nm}$. These dots have been shown to be optically inactive, due to the significant number of defects in them. The PL spectra are shown in Fig.4.2b. Notice that

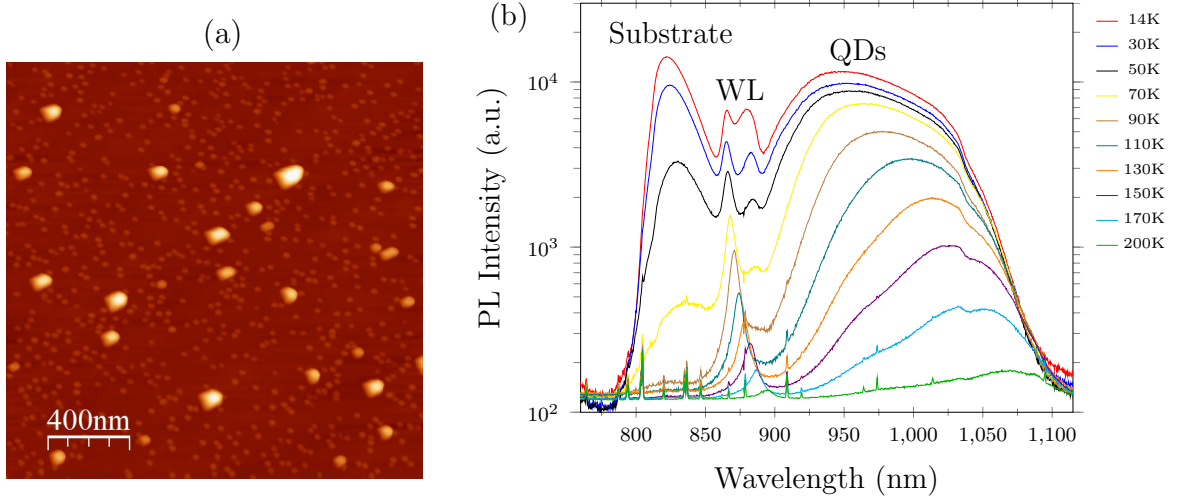


Figure 4.2: (a) The AFM result for the uncapped reference sample 1540, showing a QD density of $\sim 2 \cdot 10^{10} \text{ cm}^{-2}$, average QD height 2 – 3 nm and average diameter 40 nm. (b) The PL spectra of capped reference sample 1541.

because the bottom SSL is 100\AA apart and the top SSL is not present in these structures, the emission is red-shifted compared to the samples of Chapter 2. The relatively broad peak at around 830 nm corresponds to emission from the n^+ substrate which was used.

4.1.2 1ML AlAs capping

As a first step for the investigation, we chose to use an AlAs capping layer thickness of 1ML. It is important to have in mind that AlAs does not wet the surface on which it is grown and as a result, when we say AlAs layer thickness, we refer to the amount of AlAs deposited on the QDs, regardless of how the aluminium atoms have been arranged, forming a thin film or not. The AFM results of the uncapped sample 1543 are shown in Fig.4.3a. The QD density of the sample is reduced to $\sim 6 \cdot 10^9 \text{ cm}^{-2}$, while the dot height is slightly reduced to 2 – 2.5 nm and their diameter remains relatively intact at 40 nm. Something worth noting is that the amount of larger dots is significantly reduced, while there is a significant amount of small bumps on the surface of height below 1 nm, resembling dots that have not fully formed. The PL spectra of the capped sample 1544 is shown in Fig.4.3b. First of all, we can see that the emission intensity is lower compared to the reference samples, by almost an order of magnitude. Additionally, the QD emission seems to be somewhat blueshifted compared to the reference sample and the emission does not shift as the temperature rises as much as the reference sample with increasing.

4.1.3 0.5ML AlAs capping

Pursuing further the investigation, we decided to reduce the AlAs deposited to 0.5ML. The main reason was the reduced QD density and the presence of not fully formed dots, suggesting that the AlAs affects a posteriori the QD formation mechanism. As a result, all

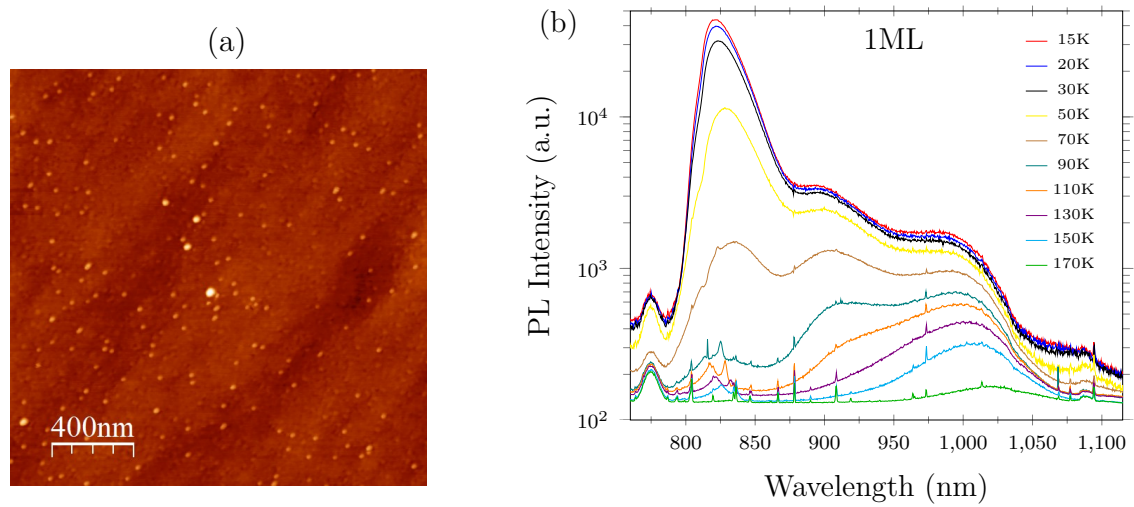


Figure 4.3: (a) The AFM results for 1543, in which the dots are capped with 1ML AlAs. The dot height and density are reduced compared to the reference sample. (b) The PL spectra of 1544, the capped version of 1543, showing weaker emission than the reference.

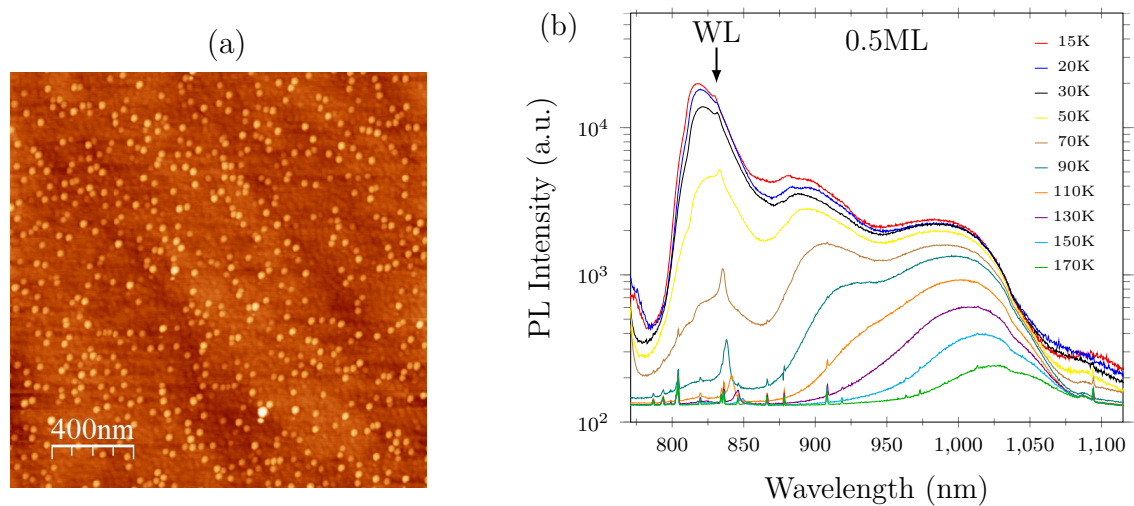


Figure 4.4: (a) The AFM results of sample 1546, where a 0.5ML AlAs capping was used. The dot height remained at 1543 levels, while the density increased to that of the reference. (b) The PL of sample 1547, which is the same as 1546, but capped. It is very similar to the PL of sample 1544 with 1ML-capping.

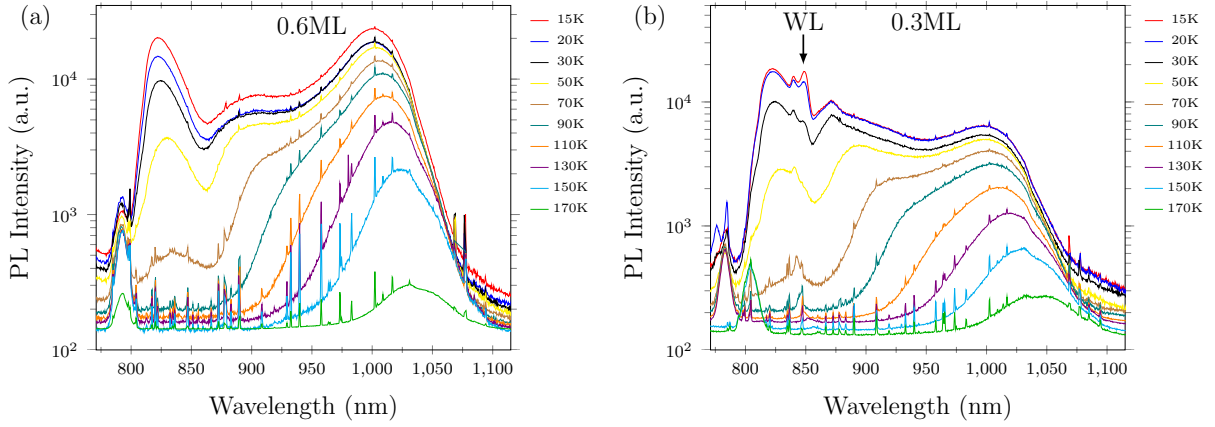


Figure 4.5: (a) The PL spectra of sample 1548, in which 0.6ML AlAs is deposited on top of the dots, showing stronger QD emission than the previous AlAs samples. (b) The PL results of sample 1549, in which the AlAs capping layer thickness was 0.3ML, showing reduced PL intensity than the reference.

of the following samples have cap layer thicknesses less than 1ML. The sample with 0.5ML AlAs on top of the dots which was left uncapped is labeled as 1546, while its capped sibling is labeled as 1547. The AFM results for the former are shown in Fig4.4. The sample is now more dense, with a QD density of $\sim 2 \cdot 10^{10} \text{ cm}^{-2}$, similar to the density of the reference sample. The height and diameter of the dots is again 2.0 – 2.5 nm and 40 nm respectively. It should be noted that the background in between dots is more rough, meaning that the overall surface has more height fluctuations, while the larger dots are absent now as well. The PL of the capped sample is shown in Fig.4.4. The spectra resemble closely the spectra of sample 1544, with the only difference being that it is slightly redshifted and it seems to hold better as the temperature rises.

4.1.4 0.6ML AlAs capping

Next, we used an AlAs capping layer of 0.6ML. Based on the trend of the AFM results, we chose not to grow an uncapped sample, assuming similar dot characteristics. The sample is labeled as 1548 and its PL characterization is shown in Fig.4.5a. As we can see, the emission is much stronger than the two previous samples by about one order of magnitude. The intensity is in fact comparable or higher to the intensity of the reference sample. The PL structure does not differ much from the other samples with AlAs capping, except for the increased intensity. This could be attributed to higher QD density or less defects. In any case, this seems like an important result. By using a 0.6ML AlAs capping layer, the PL intensity did not crumble, like the two previous samples with AlAs, but it increased slightly, at the very least.

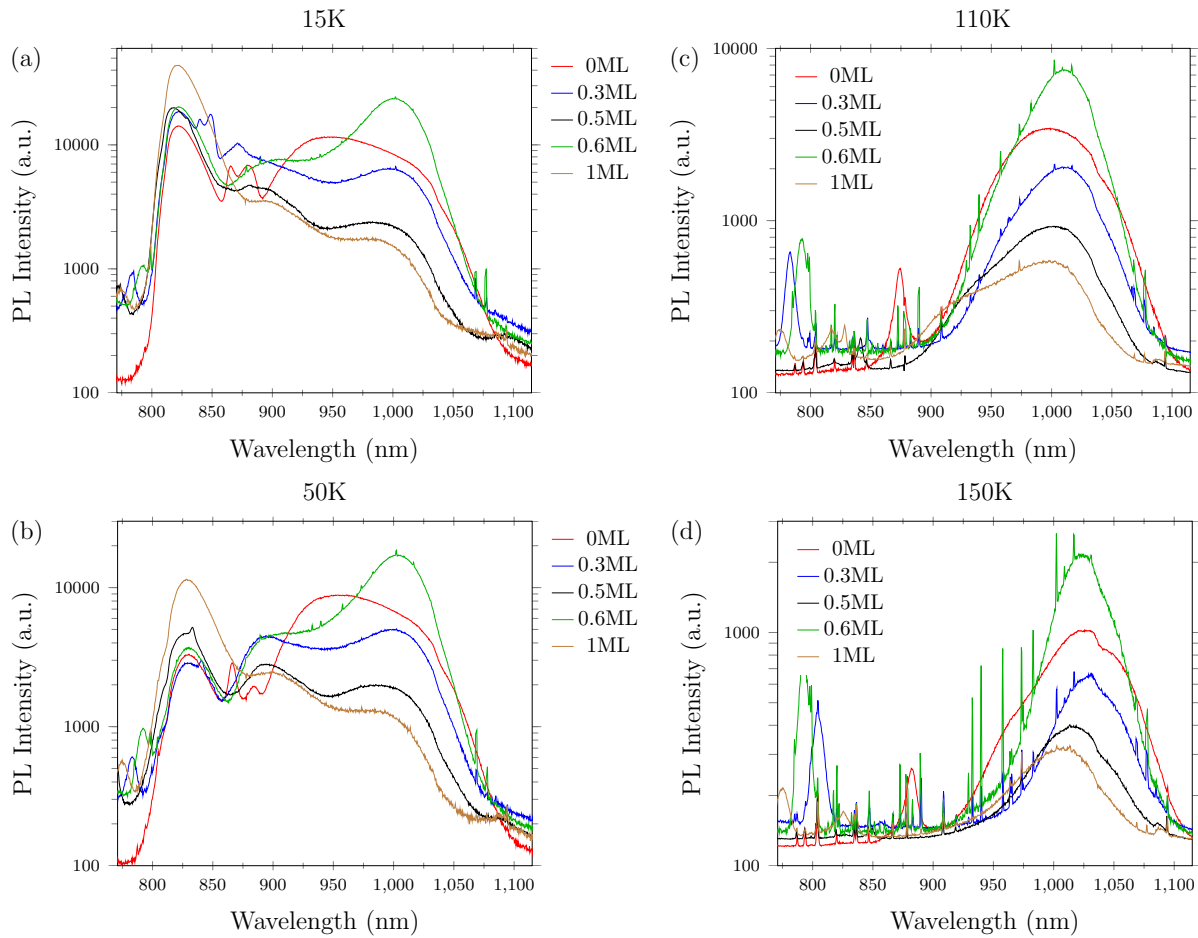


Figure 4.6: The PL comparison of the samples of the AlAs capping investigation.

4.1.5 0.3ML AlAs capping

As the final part of this investigation we checked the effect on the QD emission of the capping by 0.3ML AlAs. Again, no uncapped sample was grown for the same reasons as before. The sample is labeled as 1549 and the corresponding PL spectra are shown in Fig.4.5b. The emission intensity is reduced compared to 1548 and to the reference sample, but it is still stronger than samples 1544 and 1547. Except the intensity, the structure of the emission is similar with the rest of samples with AlAs capping, while being redshifted further.

The results of the PL characterization are summarized in Fig.4.6. First of all, with AlAs capping, the emission seems to be narrower than the reference sample, while it tends to emit in the low-energy side of the reference PL spectrum. This could mean that the QD homogeneity is improved, but it is unclear whether the relative shift is attributed to increased In composition, as it was attributed in Reference [59]. Additionally, with the exception of 0.6ML AlAs capping, the presence of AlAs reduces the PL intensity, suggesting an increase of non-radiative recombination channels when AlAs is introduced. Another result is that the WL emission is clearly affected by the deposition of AlAs. As we can see, the presence of AlAs blue-shifts the WL emission, which is a clear sign that something is happening when

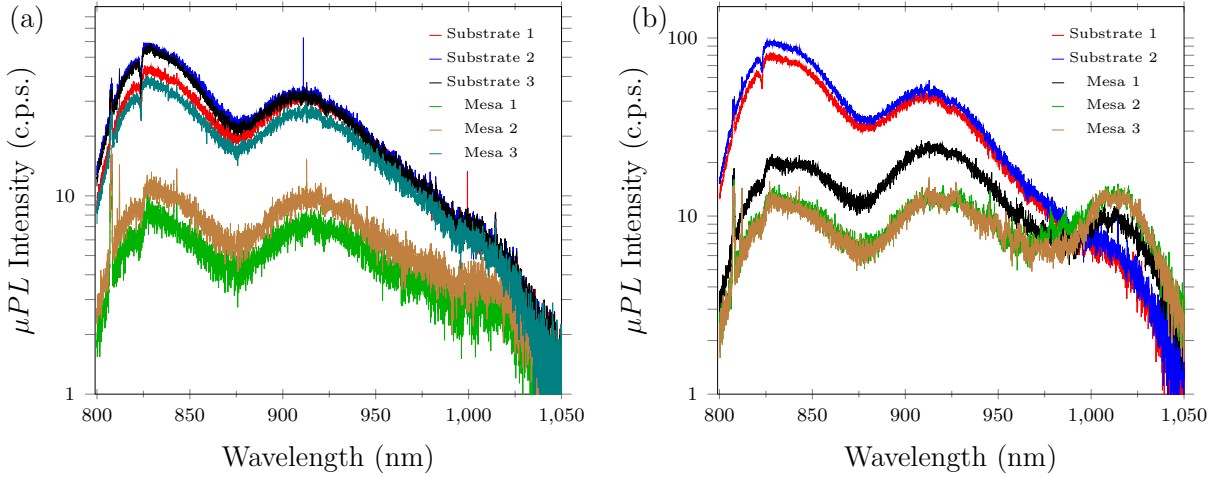


Figure 4.7: Micro-PL results from 10μ , diameter mesas of (a) sample 1544 and (b) sample 1548, showing strong background emission from the substrate, making the measurement of single dot lines impossible.

AlAs is deposited.

4.1.6 micro-PL

Based on the results presented above, we decided to perform micro-PL measurements on two of the samples. The samples that were chosen were 1544 and 1548, on which 1ML and 0.6ML AlAs have been deposited on the dots, respectively. The reason behind this decision was that the emission of the former showed blueshift compared to the reference, while the latter showed redshift, suggesting different mechanisms that take place. Keep in mind that 1544 has a weak PL, suggesting that the single-dot characterization may be more difficult due to low count of optically active QDs. However in theory, we would only need to find a few dots that emit satisfyingly to extract useful information. It is also important to keep in mind that we do not have in these samples any cavity structure and as a result the counts per second will be significantly reduced compared to the micro-PL spectra presented in Chapter 3.

For the micro-PL measurements, the diode laser emitting at 532 nm was used as the excitation source, the same as in Chapter 3. The mesas were formed using the same process flow, with the only difference that the mesa height is now $0.3 \mu\text{m}$. For details of the experimental setup and the process flow regarding the mesas formation, check Chapter 3.

The micro-PL spectra of 1544 and 1548 are shown in Fig.4.7. There, a comparison is presented, between the signal detected from the mesas and the signal detected from the substrate. The mesas used for this measurement are the ones with diameter of $10 \mu\text{m}$, i.e the largest available. As we can see, the intensity of the substrate signal is comparable or higher than the signal from the mesas and as a result no distinct quantum dot lines have been measured. Notice however, that the ratio of the peak at 830 nm to the peak at 920 nm is higher for the substrate, which indicates that there is some QD emission at $\sim 920 \text{ nm}$. This is more evident in 1548, where there is clearly also QD emission at around 1020 nm ,

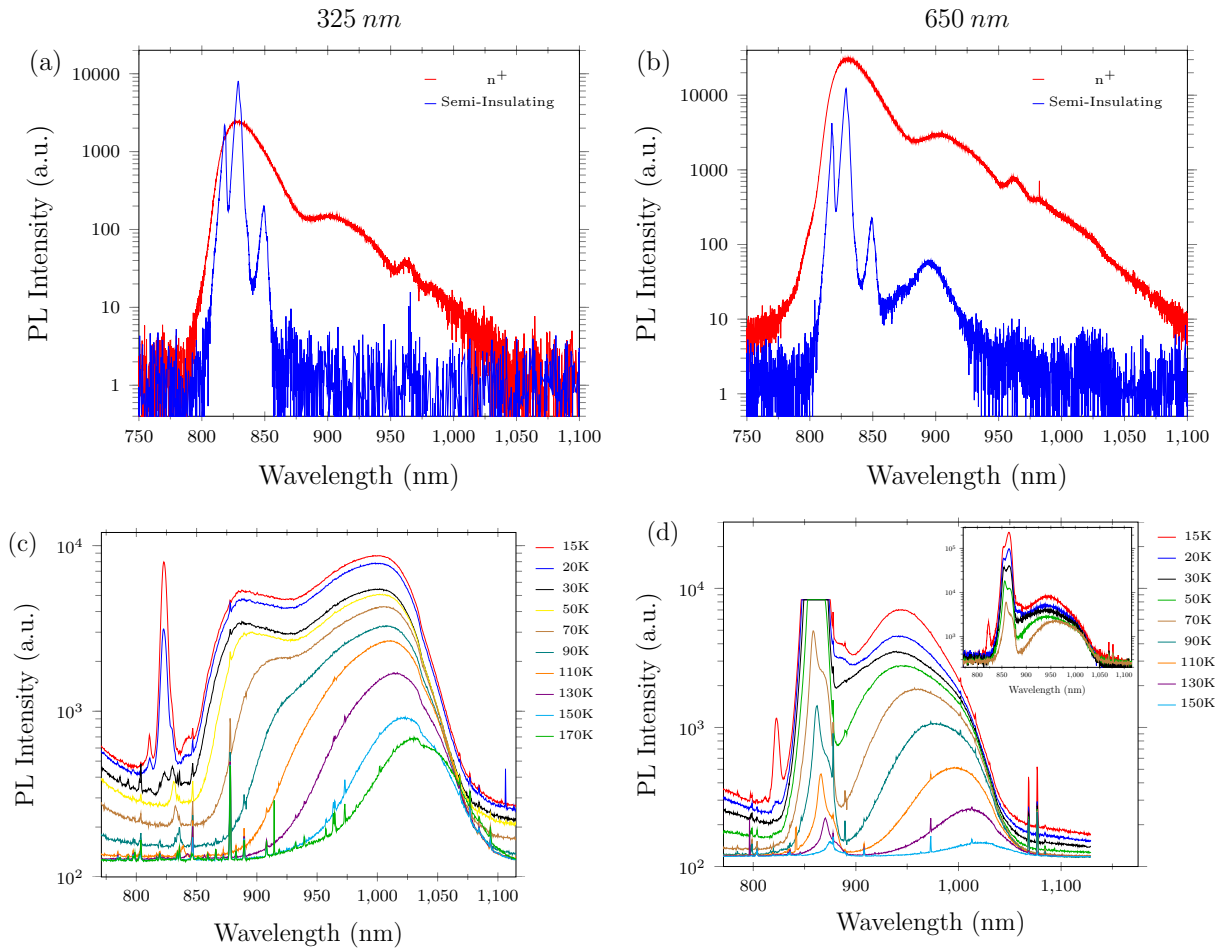


Figure 4.8: The comparison between the PL spectra of n^+ and semi-insulating substrate types for (a) 325 nm and (b) 325 nm, indicating the semi-insulating has weaker emission in the QD emission range. (c),(d) The PL spectra of samples 1567 and 1568, which feature a semi-insulating substrate.

as expected from the PL results. It is obvious that the picture is completely different from the micro-PL results presented in Chapter 3. The substrate emission is now comparable to the QD emission. This is of course something that would not have been any major issue in structures with cavity, where the dot signal is much stronger, but now, that the signal from the dots is not amplified, the measurement of single dot spectra becomes impossible.

4.1.7 AlAs-capping QD Samples on Semi-Insulating Substrates

It is clear that the substrate emission hinders the measurement of single-dot spectra. The alternative option is the substrate used in the previous chapters, which was semi-insulating (S.I.). Based on the above problems in the micro-PL measurements, we have taken a piece of the substrate wafer from both of these two substrate types and we measured their PL emission for both 325 nm and 650 nm excitation wavelengths, which is shown in Fig.4.8a and Fig.4.8b respectively. As we can see, the overall emission intensity is lower for the S.I. substrate, especially around 920 nm, where QD emission is expected based on the micro-PL

results and the . As a result, we decided to grow two new samples that are now grown on S.I. substrates.

The two new samples, labeled as 1567 and 1568, are repetitions of samples 1548 (0.6ML AlAs) and 1541 (0ML AlAs) respectively, with the substrate being the only difference. Their PL spectra is shown in Fig.4.8c and Fig.4.8d respectively. As we can see, the broad substrate peak at $\sim 830nm$ is absent in these samples. Sample 1568 has a more intense and broad WL peak than 1541, suggesting more dominant fluctuations to WL width and composition. The intensity of 1567 is slightly lower than that of 1548, which was the corresponding sample with 0.6ML AlAs with n^+ substrate. On the other hand, 1568 shows relatively weaker emission than its n^+ sibling 1541. It is now more obvious that the QD emission range is changed between the two samples. To be precise, in 1568 (0ML AlAs) the QDs emit at around $950nm$, while in 1567 (0.6ML AlAs) the dots emit at around $1000nm$. Based on the above, the single dot spectral characterization of the samples seems plausible. As a result, the samples were sent for the mesa formation. Until the writing of this thesis, the formation of the pillars was not complete and thus, no micro-PL spectra were measured, as of yet.

In this chapter, we firstly posed the issue of a reduced indium content of the dots, as revealed in Reference [19]. Next, we presented the related mechanism causing intermixing of the dots, which is called surface segregation. A possible solution to the segregation phenomena was given by the introduction of an AlAs capping layer on top of the dots and references to the literature from AlAs capping on (100) QDs were made. Finally, an experimental investigation has taken place on the effect of the AlAs capping, in which PL and AFM characterization have taken place on samples with five different AlAs capping layer thicknesses. Single dot spectra, on the other hand, were not able to be obtained using micro-PL due to background emission from the n^+ -substrate initially used.

Future Work

The work presented in this thesis are only a part of the work required to obtain and measure single-photon emitters at high temperatures. As a result, there are open topics that will be addressed in the future. Following is a concise list of the work needed to be done in the upcoming months:

- A more thorough investigation of the mesas of sample 1572, in order to find the best candidate mesas for single-photon emission at high temperatures. Some characteristics of these mesas would be that there are at most one or two QDs, the emission intensity of which is high and the excitonic and biexcitonic lines are well-defined based on thorough power dependent measurements.
- Temperature dependent measurements on sample 1572.
- Time-resolved measurements on the excitonic lines of 1572.
- Anti-bunching measurements on 1572 in order to establish the single-photon nature of the emission, at as much elevated temperature as possible.
- The micro-PL measurements of the AlAs-capped QD samples 1567 and 1568 to extract all the important quantities, related to increased In-composition in the dots, such exciton-biexciton splittings, time-decays, FSS etc.

Bibliography

- [1] M. D. Eisaman, J. Fan, A. Migdall, and S. V. Polyakov. Invited review article: Single-photon sources and detectors. *Review of Scientific Instruments*, 82(7):071101, 2011.
- [2] H. J. Kimble, M. Dagenais, and L. Mandel. Photon antibunching in resonance fluorescence. *Phys. Rev. Lett.*, 39:691–695, Sep 1977.
- [3] Th. Basché, W. E. Moerner, M. Orrit, and H. Talon. Photon antibunching in the fluorescence of a single dye molecule trapped in a solid. *Phys. Rev. Lett.*, 69:1516–1519, Sep 1992.
- [4] Christian Kurtsiefer, Sonja Mayer, Patrick Zarda, and Harald Weinfurter. Stable solid-state source of single photons. *Phys. Rev. Lett.*, 85:290–293, Jul 2000.
- [5] P. Michler, A. Kiraz, C. Becher, W. V. Schoenfeld, P. M. Petroff, Lidong Zhang, E. Hu, and A. Imamoglu. A quantum dot single-photon turnstile device. *Science*, 290(5500):2282–2285, 2000.
- [6] G. Liu, A. Stintz, H. Li, K. J. Malloy, and L. F. Lester. Extremely low room-temperature threshold current density diode lasers using InAs dots in $\text{In}_{0.15}\text{Ga}_{0.85}\text{As}$ quantum well. *Electronics Letters*, 35(14):1163–1165, Jul 1999.
- [7] O. Fedorych, C. Kruse, A. Ruban, D. Hommel, G. Bacher, and T. Kmmell. Room temperature single photon emission from an epitaxially grown quantum dot. *Applied Physics Letters*, 100(6):061114, 2012.
- [8] Mark J. Holmes, Kihyun Choi, Satoshi Kako, Munetaka Arita, and Yasuhiko Arakawa. Room-temperature triggered single photon emission from a III-Nitride site-controlled nanowire quantum dot. *Nano Letters*, 14(2):982–986, 2014. PMID: 24422516.
- [9] Richard P. Mirin. Photon antibunching at high temperature from a single InGaAs/GaAs quantum dot. *Applied Physics Letters*, 84(8):1260–1262, 2004.
- [10] X. M. Dou, X. Y. Chang, B. Q. Sun, Y. H. Xiong, Z. C. Niu, S. S. Huang, H. Q. Ni, Y. Du, and J. B. Xia. Single-photon-emitting diode at liquid nitrogen temperature. *Applied Physics Letters*, 93(10):101107, 2008.
- [11] R. J. Young, R. M. Stevenson, A. J. Shields, P. Atkinson, K. Cooper, D. A. Ritchie, K. M. Groom, A. I. Tartakovskii, and M. S. Skolnick. Inversion of exciton level splitting in quantum dots. *Phys. Rev. B*, 72:113305, Sep 2005.

-
- [12] M. Bayer, G. Ortner, O. Stern, A. Kuther, A. A. Gorbunov, A. Forchel, P. Hawrylak, S. Fafard, K. Hinzer, T. L. Reinecke, S. N. Walck, J. P. Reithmaier, F. Klopff, and F. Schäfer. Fine structure of neutral and charged excitons in self-assembled In(Ga)As/(Al)GaAs quantum dots. *Phys. Rev. B*, 65:195315, May 2002.
- [13] A. J. Bennett, M. A. Pooley, R. M. Stevenson, M. B. Ward, R. B. Patel, A. Boyer de la Giroday, N. Skold, I. Farrer, C. A. Nicoll, D. A. Ritchie, and A. J. Shields. Electric-field-induced coherent coupling of the exciton states in a single quantum dot. *Nat Phys*, 6(12):947–950, Dec 2010.
- [14] J. D. Plumhof, V. Křápek, F. Ding, K. D. Jöns, R. Hafenbrak, P. Klenovský, A. Herklotz, K. Dörr, P. Michler, A. Rastelli, and O. G. Schmidt. Strain-induced anticrossing of bright exciton levels in single self-assembled GaAs/Al_xGa_{1-x}As and In_xGa_{1-x}As/GaAs quantum dots. *Phys. Rev. B*, 83:121302, Mar 2011.
- [15] A. Mohan, M. Felici, P. Gallo, B. Dwir, A. Rudra, J. Faist, and E. Kapon. Polarization-entangled photons produced with high-symmetry site-controlled quantum dots. *Nat Photon*, 4(5):302–306, May 2010.
- [16] Claus F. Klingshirn. *Excitons, Biexcitons and Trions*, pages 249–271. Springer Berlin Heidelberg, Berlin, Heidelberg, 2012.
- [17] I. N. Stranski and L. Krastanow. Zur theorie der orientierten ausscheidung von ionenkristallen aufeinander. *Monatshefte für Chemie und verwandte Teile anderer Wissenschaften*, 71(1):351–364, Dec 1937.
- [18] G. E. Dialynas, S. Kalliakos, C. Xenogianni, M. Androulidaki, T. Kehagias, P. Komninou, P. G. Savvidis, Z. Hatzopoulos, and N. T. Pelekanos. Piezoelectric InAs (211)B quantum dots grown by molecular beam epitaxy: Structural and optical properties. *Journal of Applied Physics*, 108(10):103525, 2010.
- [19] N. Florini, G. P. Dimitrakopoulos, J. Kioseoglou, S. Germanis, C. Katsidis, Z. Hatzopoulos, N. T. Pelekanos, and Th. Kehagias. Structure, strain, and composition profiling of InAs/GaAs(211)B quantum dot superlattices. *Journal of Applied Physics*, 119(3):034304, 2016.
- [20] R. Seguin, A. Schliwa, S. Rodt, K. Pötschke, U. W. Pohl, and D. Bimberg. Size-dependent fine-structure splitting in self-organized InAs/GaAs quantum dots. *Phys. Rev. Lett.*, 95:257402, Dec 2005.
- [21] Andrei Schliwa, Momme Winkelkemper, Anatol Lochmann, Erik Stock, and Dieter Bimberg. In(Ga)As/GaAs quantum dots grown on a (111) surface as ideal sources of entangled photon pairs. *Phys. Rev. B*, 80:161307, Oct 2009.
- [22] D. Bimberg, E. Stock, A. Lochmann, A. Schliwa, J. A. Tofflinger, W. Unrau, M. Munnix, S. Rodt, V. A. Haisler, A. I. Toropov, A. Bakarov, and A. K. Kalagin. Quantum dots for single- and entangled-photon emitters. *IEEE Photonics Journal*, 1(1):58–68, June 2009.

-
- [23] D. L. Smith and C. Mailhot. Piezoelectric effects in strained-layer superlattices. *Journal of Applied Physics*, 63(8):2717–2719, 1988.
- [24] Erik Stock, Till Warming, Irina Ostapenko, Sven Rodt, Andrei Schliwa, Jan Amaru Tfflinger, Anatol Lochmann, Aleksandr I. Toropov, Sergej A. Moshchenko, Dimitry V. Dmitriev, Vladimir A. Haisler, and Dieter Bimberg. Single-photon emission from In-GaAs quantum dots grown on (111) GaAs. *Applied Physics Letters*, 96(9):093112, 2010.
- [25] G. Arlt and P. Quadflieg. Piezoelectricity in III-V compounds with a phenomenological analysis of the piezoelectric effect. *physica status solidi (b)*, 25(1):323–330, 1968.
- [26] S. Birner, T. Zibold, T. Andlauer, T. Kubis, M. Sabathil, A. Trellakis, and P. Vogl. nextnano: General purpose 3-D simulations. *IEEE Transactions on Electron Devices*, 54(9):2137–2142, Sept 2007.
- [27] S. Germanis, A. Beveratos, K. Gauthron, A. Stavrinidis, G. Konstantinidis, Z. Hatzopoulos, and N.T. Pelekanos. Recombination dynamics in piezoelectric (211)B InAs quantum dots. *Microelectronic Engineering*, 112:179 – 182, 2013.
- [28] Y.P. Varshni. Temperature dependence of the energy gap in semiconductors. *Physica*, 34(1):149 – 154, 1967.
- [29] Fang Yang, M. Wilkinson, E. J. Austin, and K. P. O’Donnell. Origin of the Stokes shift: A geometrical model of exciton spectra in 2D semiconductors. *Phys. Rev. Lett.*, 70:323–326, Jan 1993.
- [30] Kerry J. Vahala. Optical microcavities. *Nature*, 424(6950):839–846, Aug 2003.
- [31] Julien Claudon, Joel Bleuse, Nitin Singh Malik, Maela Bazin, Perine Jaffrennou, Niels Gregersen, Christophe Sauvan, Philippe Lalanne, and Jean-Michel Gérard. A highly efficient single-photon source based on a quantum dot in a photonic nanowire. *Nat Photon*, 4(3):174–177, Mar 2010.
- [32] Subir Sachdev. Atom in a damped cavity. *Phys. Rev. A*, 29:2627–2633, May 1984.
- [33] Lambropoulos Peter and David Petrosyan. *Cavity Quantum Electrodynamics*, pages 151–177. Springer Berlin Heidelberg, Berlin, Heidelberg, 2007.
- [34] Marlan O. Scully and M. Suhail Zubairy. *Quantum Optics*:. Cambridge University Press, 1997.
- [35] J. P. Reithmaier, G. Sek, A. Löffler, C. Hofmann, S. Kuhn, S. Reitzenstein, L. V. Keldysh, V. D. Kulakovskii, T. L. Reinecke, and A. Forchel. Strong coupling in a single quantum dot-semiconductor microcavity system. *Nature*, 432(7014):197–200, Nov 2004.
- [36] E. M. Purcell, H. C. Torrey, and R. V. Pound. Resonance absorption by nuclear magnetic moments in a solid. *Phys. Rev.*, 69:37–38, Jan 1946.

-
- [37] P Lambropoulos, Georgios M Nikolopoulos, Torben R Nielsen, and Sren Bay. Fundamental quantum optics in structured reservoirs. *Reports on Progress in Physics*, 63(4):455, 2000.
- [38] W.-Y. Chen, H.-S. Chang, T. M. Hsu, T.-P. Hsieh, and J.-I. Chyi. Temperature stability of single-photon emission from InGaAs quantum dots in photonic crystal nanocavities. *Applied Physics Letters*, 90(21):211114, May 2007.
- [39] Yoshihisa Yamamoto, Susumu Machida, and G. Björk. Micro-cavity semiconductor lasers with controlled spontaneous emission. *Optical and Quantum Electronics*, 24(2):S215–S243, Feb 1992.
- [40] Gunnar Björk, Yoshihisa Yamamoto, and Henrich Heitmann. *Spontaneous Emission Control in Semiconductor Microcavities*, pages 467–501. Springer US, Boston, MA, 1995.
- [41] T. Baba, T. Hamano, F. Koyama, and K. Iga. Spontaneous emission factor of a micro-cavity DBR surface-emitting laser. *IEEE Journal of Quantum Electronics*, 27(6):1347–1358, Jun 1991.
- [42] Nowicki-Bringuier, Y.-R., Hahner, R., Claudon, J., Lecamp, G., Lalanne, P., and Gérard, J. M. A novel high-efficiency single-mode single photon source. *Ann. Phys. Fr.*, 32(2), 2007.
- [43] A. J. Bennett, P. Atkinson, P. See, M. B. Ward, R. M. Stevenson, Z. L. Yuan, D. C. Unitt, D. J. P. Ellis, K. Cooper, D. A. Ritchie, and A. J. Shields. Single-photon-emitting diodes: a review. *physica status solidi (b)*, 243(14):3730–3740, 2006.
- [44] S.A. Furman and A.V. Tikhonravov. *Basics of Optics of Multilayer Systems*. Basics of Optics of Multilayer Systems. Editions Frontières, 1992.
- [45] I. Friedler, C. Sauvan, J. P. Hugonin, P. Lalanne, J. Claudon, and J. M. Gérard. Solid-state single photon sources: the nanowire antenna. *Opt. Express*, 17(4):2095–2110, Feb 2009.
- [46] R. G. Neuhauser, K. T. Shimizu, W. K. Woo, S. A. Empedocles, and M. G. Bawendi. Correlation between fluorescence intermittency and spectral diffusion in single semiconductor quantum dots. *Phys. Rev. Lett.*, 85:3301–3304, Oct 2000.
- [47] K. T. Shimizu, R. G. Neuhauser, C. A. Leatherdale, S. A. Empedocles, W. K. Woo, and M. G. Bawendi. Blinking statistics in single semiconductor nanocrystal quantum dots. *Phys. Rev. B*, 63:205316, May 2001.
- [48] Christophe Galland, Yagnaseni Ghosh, Andrea Steinbruck, Milan Sykora, Jennifer A. Hollingsworth, Victor I. Klimov, and Han Htoon. Two types of luminescence blinking revealed by spectroelectrochemistry of single quantum dots. *Nature*, 479(7372):203–207, Nov 2011.

- [49] L. Vegard. Die konstitution der mischkristalle und die raumfüllung der atome. *Zeitschrift für Physik*, 5(1):17–26, Jan 1921.
- [50] Gabriel Bester, Xifan Wu, David Vanderbilt, and Alex Zunger. Importance of second-order piezoelectric effects in zinc-blende semiconductors. *Phys. Rev. Lett.*, 96:187602, May 2006.
- [51] J. M. Moison, C. Guille, F. Houzay, F. Barthe, and M. Van Rompay. Surface segregation of third-column atoms in group III-V arsenide compounds: Ternary alloys and heterostructures. *Phys. Rev. B*, 40:6149–6162, Sep 1989.
- [52] A. Rosenauer, D. Gerthsen, D. Van Dyck, M. Arzberger, G. Böhm, and G. Abstreiter. Quantification of segregation and mass transport in $\text{In}_x\text{Ga}_{1-x}\text{As}/\text{GaAs}$ Stranski-Krastanow layers. *Phys. Rev. B*, 64:245334, Dec 2001.
- [53] A Sher, M A Berding, M van Schilfgaarde, and An-Ban Chen. HgCdTe status review with emphasis on correlations, native defects and diffusion. *Semiconductor Science and Technology*, 6(12C):C59, 1991.
- [54] K. Muraki, S. Fukatsu, Y. Shiraki, and R. Ito. Surface segregation of In atoms during molecular beam epitaxy and its influence on the energy levels in InGaAs/GaAs quantum wells. *Applied Physics Letters*, 61(5):557–559, 1992.
- [55] M. Schowalter, A. Rosenauer, D. Gerthsen, M. Arzberger, M. Bichler, and G. Abstreiter. Investigation of In segregation in InAs/AlAs quantum-well structures. *Applied Physics Letters*, 79(26):4426–4428, 2001.
- [56] Ch. Heyn, A. Bolz, T. Maltezopoulos, R.L. Johnson, and W. Hansen. Intermixing in self-assembled InAs quantum dot formation. *Journal of Crystal Growth*, 278(1):46 – 50, 2005. 13th International Conference on Molecular Beam Epitaxy.
- [57] Jean-Michel Gérard and Cécile d’Anterrosches. Growth of InGaAs/GaAs heterostructures with abrupt interfaces on the monolayer scale. *Journal of Crystal Growth*, 150(Part 1):467 – 472, 1995.
- [58] S.Yu Karpov and Yu.N Makarov. Indium segregation kinetics in InGaAs ternary compounds. *Thin Solid Films*, 380(1):71 – 74, 2000.
- [59] M. Arzberger, U. Käsberger, G. Böhm, and G. Abstreiter. Influence of a thin AlAs cap layer on optical properties of self-assembled InAs/GaAs quantum dots. *Applied Physics Letters*, 75(25):3968–3970, 1999.
- [60] H. Yokota, K. Iizuka, H. Okamoto, and T. Suzuki. AlAs coating for stacked structure of self-assembled InAs/GaAs quantum dots. *Journal of Crystal Growth*, 301(Supplement C):825 – 827, 2007. 14th International Conference on Molecular Beam Epitaxy.
- [61] V. G. Dorogan, Yu. I. Mazur, J. H. Lee, Zh. M. Wang, M. E. Ware, and G. J. Salamo. Thermal peculiarity of AlAs-capped InAs quantum dots in a GaAs matrix. *Journal of Applied Physics*, 104(10):104303, 2008.

